On Characterization and Augmentation of Coupled Phased Array for Antenna Scanning

by

Kaiyue Zhang

A Dissertation Presented in Partial Fulfillment
of the Requirements for the Degree
Doctor of Philosophy

Approved April 2023 by the
Graduate Supervisory Committee:

George Pan, Chair
Hongbin Yu
James Aberle
Joseph Palais

ARIZONA STATE UNIVERSITY

May 2023

ABSTRACT

Antenna arrays are widely used in wireless communication, radar, remote sensing, and other fields. Compared to traditional linear antenna arrays, novel nonlinear antenna arrays have fascinating advantages in terms of structural simplicity, lower cost, wider bandwidth, faster scanning speed, and lower side-lobe levels. This dissertation explores a novel design of a phased array antenna with an augmented scanning range, aiming to establish a clear connection between mathematical principles and practical circuitry. To achieve this goal, the Van der Pol (VDP) model is applied to a single-transistor oscillator to obtain the isolated limit cycle. The coupled oscillators are then integrated into a 1×7 coupled phased array, using the Keysight PathWave Advanced Design System (ADS) for tuning and optimization. The VDP model is used for analytic study of bifurcation, quasi-sinusoidal oscillation, quasi-periodic chaos, and oscillator death, while ADS schematics guide engineering implementation and physical fabrication. The coupled oscillators drive cavity-backed antennas, forming a 1D scanning antenna array of 1×7. The approaches for increasing the scanning range performance are discussed.

ACKNOWLEDGMENTS

I would like to express my heartfelt gratitude to my mentor and guide, Dr. George Pan. Your valuable insights, guidance, and boundless encouragement have been instrumental in shaping my academic journey and research project.

I am also grateful to my committee members, Dr. Hongbin Yu, Dr. James Aberle, and Dr. Joseph Palais, for their insightful advice and extensive knowledge that greatly contributed to the development of my research.

I would like to extend my thanks to my girlfriend, Yaru Yang, and our family, who have been my pillars of strength throughout this journey. Your unconditional love, unwavering support, and profound understanding have been the driving force behind my success.

Thank you all for your invaluable contributions to my academic pursuits.

TABLE OF CONTENTS

Page

LIST OF TABLES

LIST OF FIGURES

Figure Page

Chapter 1

INTRODUCTION

Antenna technology has come a long way since its inception in the early 20th century. From simple wire loops to complex multi-element arrays, antennas have become an essential part of modern communication systems. Antenna arrays have been widely used in wireless communication, radar, remote sensing, among others [1].

Nonlinear antenna technology is a relatively new field that aims to improve the performance of antennas in the presence of nonlinear loads and complex modulation schemes. When comparing traditional linear antenna arrays with novel nonlinear antenna arrays, the latter exhibit fascinating advantages in terms of structural simplicity, lower cost, wider bandwidth, faster scanning speed, and lower side-lobe levels [2]. Nonlinear antenna technology combines advances in nonlinear dynamics, active antenna design, and analog microelectronics to achieve beam steering and beam forming using an array of nonlinear oscillators [3–5]. This technology utilizes two phenomena that are typically avoided in traditional designs: nonlinear unit cells and inter-element coupling.

Nonlinear antennas can be implemented with space-time varying metasurfaces, synchronized radiating systems, fast switch-controlled modulations, and nonlinear materials. However, the coupled oscillator phased array (COPA) approach overwhelmingly dominates [6], with 120 references provided. Following Adler's pioneering paper [7], significant contributions have been made in COPA by [8–11]. Mathematically, COPA, as a nonlinear device, is a branch of nonlinear dynamics [12]. Stable limit cycles (SLCs) appearing in nonlinear systems have minimum energy or have no external

periodic force. For antenna circuitry, assuming the non-linearity is the same as the Van der Pol oscillator, the Poincare-Bendixson theorem [13] guarantees the occurrence of the required SLCs on the unstable central manifolds through the Hopf bifurcation. Integer-valued Lyapunov can be applied. Applied mathematicians have developed novel formulations to obtain the required periodic signals for the SLCs and work on the linear evolution equation initial value problem, assuming the coefficient matrix has a compact resolvent, and generates the exponentially-stable solution semi-group. The existence and stability conditions and an optimized estimate can be obtained for the linear case [12, 14].

In this paper, we will delve into the concerns, design, and optimization of the oscillator and antenna components. In Chapter 2, the designs of Radio Frequency (RF) oscillators are discussed [15–19]. A push-pull oscillator operating at 10 GHz is presented and ready to be utilized as the source of the phased array antennas. In Chapter 3, different types of antenna elements are analyzed and considered as candidate components for the phased array system. The horn antenna is designed, optimized, and built with 3-D printing technology [20]. A cavity-backed slotted antenna [21] is modeled and optimized by scaling electrical size [22]. The formulation of equivalent waveguide size is studied. A more sophisticated design of cavity-backed slot array is studied, simulated, and modified. After rebuilding layers of the antenna, several modification approaches are conducted. The phased oscillator array is then combined with the antenna array. The scanning range is investigated, and then the methods of increasing the scanning range are discussed.

1.1 The Van der Pol Equation and Method

The Van der Pol equation,

$$x'' - \varepsilon(1 - x^2)x' + x = 0 \tag{1.1}$$

is a nonlinear differential equation that has been used to model a wide range of physical phenomena. It is an important mathematical technique used to describe and analyze the behavior of nonlinear oscillating systems. The Van der Pol equation can be used to model the behavior of a wide range of oscillating systems, including oscillators in electrical circuits.

The Van der Pol method is particularly useful for analyzing and predicting the behavior of oscillating systems that exhibit nonlinear behavior, such as hysteresis or bi-stability. It can also be used to analyze the stability and bifurcation behavior of oscillating systems, which is important for understanding how these systems respond to external perturbations [23, 24]. In this section, the relationship between the Van der Pol equation and a resonance circuit will be derived firstly.

1.1.1 Van der Pol Equation from a Resonant Circuit

The Van der Pol equation is well-known for its ability to exhibit limit cycle behavior, making it a valuable tool for studying nonlinear dynamics. By understanding the relationship between this equation and a resonance circuit, a deeper insight into the behavior of oscillators will be helpful for developing more efficient and accurate synchronization methods.

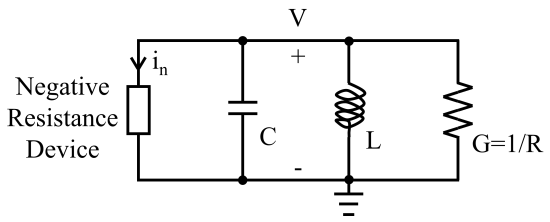

Figure 1. An Equivalent Model of Resonance Circuit, Which Contains Negative Resistance Component.

Apply Kirchhoff's current law to Figure 1:

$$I_n + V(j\omega C + \frac{1}{j\omega L}) + GV = 0. \tag{1.2}$$

It's differential equation form is:

$$\begin{aligned} & i_n + C\frac{\mathrm{d}v}{\mathrm{d}t} + \frac{1}{L}\int v\mathrm{d}t + Gv = 0 \\ \Rightarrow \quad & \frac{\mathrm{d}^2v}{\mathrm{d}t^2} + \frac{1}{C}(\frac{\mathrm{d}i_n}{\mathrm{d}v} + G)\frac{\mathrm{d}v}{\mathrm{d}t} + \frac{v}{LC} = 0. \end{aligned} \tag{1.3}$$

For many active devices, a cubic non-linearity is common, therefore the electric current can be written as:

$$i_n = -av + bv^3 \tag{1.4}$$

where a and b are positive constants. Take (1.4) into (1.3) and rewrite $\frac{\mathrm{d}v}{\mathrm{d}t}$ in a simple form $\dot{v}$:

$$\ddot{v} + \frac{1}{C}(-a + 3bv^2 + G)\dot{v} + \frac{v}{LC} = 0. \tag{1.5}$$

Note that $\frac{1}{LC} = \omega_0^2$, and let $\tau = \omega_0 t$, thus $\frac{\mathrm{d}}{\mathrm{d}\tau} = \frac{\mathrm{d}}{\omega_0 \mathrm{d}t}$. The derivatives are:

$$\begin{aligned} \ddot{v} &= \omega_0^2 \frac{\mathrm{d}^2v}{\mathrm{d}\tau^2} \\ \dot{v} &= \omega_0 \frac{\mathrm{d}v}{\mathrm{d}\tau}. \end{aligned} \tag{1.6}$$

Substitute (1.6) to (1.5):

$$\omega_0^2 \frac{\mathrm{d}^2v}{\mathrm{d}\tau^2} - \frac{1}{\omega_0 C}\left[(a - G) - 3bv^2\right]\omega_0 \frac{\mathrm{d}v}{\mathrm{d}\tau} + \omega_0^2 v = 0. \tag{1.7}$$

Equation (1.7) resembles to the Van der Pol equation, (1.1), but needs some coefficient variations. Let $x = kv, \omega_0 \frac{\mathrm{d}v}{\mathrm{d}\tau} = v'$, thus $x' = kv', x'' = kv''$. The Van der Pol equation can be rewritten as:

$$\begin{aligned} & kv'' - \varepsilon(1 - k^2v^2)kv' + kv = 0 \\ \Rightarrow \quad & v'' - \varepsilon(1 - k^2v^2)v' + v = 0. \end{aligned} \tag{1.8}$$

Replace the coefficients with parameters from the practical circuit:

$$v'' - \frac{a - G}{\omega_0 C}(1 - \frac{3b}{a - G}v^2)v' + v = 0 \tag{1.9}$$

where $\varepsilon = \frac{a-G}{\omega_0 C}, k = \sqrt{\frac{3b}{a-G}}$. The derivation above presents the discovery of the relationship between the Van der Pol equation and the circuit.

1.1.2 Solution of No Resonance

The conditions of resonance and no resonance are discussed.

$$\ddot{x}\left(t\right) - \varepsilon\left(1 - x^2\left(t\right)\right)\dot{x}\left(t\right) + x\left(t\right) = 0. \tag{1.10}$$

The perturbation with first order approximation will be applied in this subsection. If the initial condition is regulated to be $x^2(0) + \dot{x}^2 = 4$, the resonance will be eliminated. For designs of oscillator, the stable solution aforementioned should be avoid carefully.c

The initial conditions are $x(0) = \varphi$ and $\dot{x}(0) = \xi$. If $\varepsilon \ll 1$, the equation becomes $\ddot{x}_0 + x_0 = 0$, which has an exact solution,

$$x(t) = x_0(t) + \varepsilon x_1(t) + \varepsilon^2 x_2(t) + \cdots . \tag{1.11}$$

Thus, the first-order approximation results in,

$$x(t) = x_0(t) + \varepsilon x_1(t). \tag{1.12}$$

To determine $x_0(t)$ and $x_1(t)$, substitute Equation 1.12 into Equation 1.10,

$$\begin{aligned}(\ddot{x}_0 + x_0) + \varepsilon(\ddot{x}_1 - \dot{x}_0 + x_0^2\dot{x}_0 + x_1) + \varepsilon^2(x_0^2\dot{x}_1 + 2x_1x_0\dot{x}_0 - \dot{x}_1) \\ + \varepsilon^3(x_1^2\dot{x}_0 + 2x_1x_0\dot{x}_1) + \varepsilon^4 x_1^2\dot{x}_1 = 0. \end{aligned} \tag{1.13}$$

Again, make the first-order approximation and two terms left,

$$(\ddot{x}_0 + x_0) + \varepsilon(\ddot{x}_1 - \dot{x}_0 + x_0^2\dot{x}_0 + x_1) = 0. \tag{1.14}$$

It implies that the two term are equal to zero respectively:

$$\ddot{x}_0 + x_0 = 0 \tag{1.15}$$

and

$$\ddot{x}_1 - \dot{x}_0 + x_0^2\dot{x}_0 + x_1 = 0. \tag{1.16}$$

The solution of Equation 1.15 is:

$$x_0(t) = A_0 \cos t + B_0 \sin t. \tag{1.17}$$

By assuming the initial conditions of $x_1(t)$ are zero, the parameters can be solved by take to the $x(t)$.

$$x_0(t) = \varphi \cos t + \xi \sin t \tag{1.18}$$

Substituting the solution above into Equation 1.16, the equation is expanded to,

$$\begin{aligned}\ddot{x}_1 + x_1 = &- \varphi \sin t + \xi \cos t - \xi^3 \cos t \sin^2 t - 2\xi^2\varphi \cos^2 t \sin t + \xi^2\varphi \sin^3 t \\ &- \xi\varphi^2 \cos^3 t + 2\xi\varphi^2 \cos t \sin^2 t + \varphi^3 \cos^2 t \sin t. \end{aligned} \tag{1.19}$$

Using $\sin t \cos^2 t = \frac{1}{4}(\sin t + \sin 3t)$ and $\cos t \sin^2 t = \frac{1}{4}(\cos t - \cos 3t)$, the equation can be simplified to:

$$\begin{aligned}\ddot{x}_1 + x_1 = &\left(-\varphi - \frac{\xi^2\varphi}{2} + \frac{\varphi^3}{4}\right)\sin t + \left(\xi - \frac{\xi^3}{4} + \frac{\xi\varphi^2}{2}\right)\cos t + \left(\frac{\xi^3}{4} - \frac{\xi\varphi^2}{2}\right)\cos 3t \\ &+ \left(-\frac{\xi^2\varphi}{2} + \frac{\varphi^3}{4}\right)\sin 3t + \xi\varphi\left(\xi \sin^3 t - \varphi \cos^3 t\right). \end{aligned} \tag{1.20}$$

According to trigonometric identities, the cubic terms can be further simplified.

$$\xi \sin^3 t - \varphi \cos^3 t = \frac{1}{4}\left(-3\varphi \cos t - \varphi \cos 3t + 3\xi \sin t - \xi \sin 3t\right) \tag{1.21}$$

$$\begin{aligned}
\ddot{x}_1 + x_1 &= \left(-\varphi - \frac{\xi^2\varphi}{2} + \frac{\varphi^3}{4} + \frac{3\xi^2\varphi}{4}\right)\sin t + \left(\xi - \frac{\xi^3}{4} + \frac{\xi\varphi^2}{2} - \frac{3\xi\varphi^2}{4}\right)\cos t \\
&\quad + \left(\frac{\xi^3}{4} - \frac{\xi\varphi^2}{2} - \frac{\xi\varphi^2}{4}\right)\cos 3t + \left(-\frac{\xi^2\varphi}{2} + \frac{\varphi^3}{4} - \frac{\xi^2\varphi}{4}\right)\sin 3t \\
&= \varphi\left(-1 + \frac{\varphi^2+\xi^2}{4}\right)\sin t + \xi\left(1 - \frac{\varphi^2+\xi^2}{4}\right)\cos t \\
&\quad + \xi\left(\frac{-3\varphi^2+\xi^2}{4}\right)\cos 3t + \varphi\left(\frac{\varphi^2-3\xi^2}{4}\right)\sin 3t.
\end{aligned} \tag{1.22}$$

If the initial conditions are restricted as $\xi^2+\varphi^2 = 4$, the first order forcing functions in Equation 1.22 are vanished. The result in this case is not resonant.

To solve the equation, it is assumed to have one homogeneous solution and two particular solutions, $x_1(t) = x_{1,h} + x_{1,p1} + x_{1,pw}$. With the initial conditions applied, $x_1(0) = 0$ and $\dot{x}_1 = 0$.

Therefore, the first-order perturbation solution is,

$$\begin{aligned}
x(t) &= x_0(t) + \varepsilon x_1(t) \\
&= \varphi\cos t + \xi \sin t + \varepsilon\left(\frac{\xi(\xi^2-3)}{8}\cos t + \frac{3\varphi(\varphi^2-3)}{8}\sin t\right. \\
&\quad \left. + \frac{\xi(-\xi^2+3)}{8}\cos 3t + \frac{\varphi(-\varphi^2+3)}{8}\sin 3t\right).
\end{aligned} \tag{1.23}$$

The solution above is restricted by a small value of ε, and the initial condition $\varphi^2 + \xi^2 = x^2(0) + \dot{x}^2(0) = 4$.

The phase plot of no resonance case is presented in Figure 2. The initial values are selected as $x(0) = 1.5$ and $\dot{x}(0) = \sqrt{4 - x(0)}$.

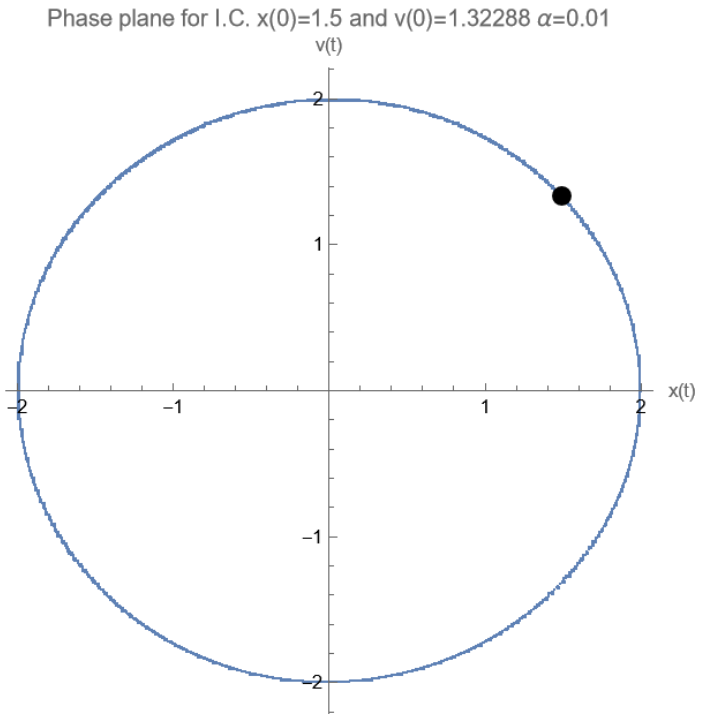

Figure 2. Phase Plot of No Resonance Case

1.1.3 Solution of Resonance

The solving and simplification procedures are similar to the previous subsection. However, it is slightly difficult to guess the form of the particular solutions of the first-order component, $x_1(t)$. This solution is still derived according to the first-order approximation, the much more complicated high-order solutions are ignored due to the small value of ε. Without the restriction of $\xi^2 + \varphi^2 = 4$, four particular solutions

of equation 1.22 exists.

$$x_{1,p1} = \left(1 - \frac{\varphi^2 + \xi^2}{4}\right) \frac{\varphi t \cos t}{2} \tag{1.24}$$

$$x_{1,p2} = \left(1 + \frac{\varphi^2 - \xi^2}{4}\right) \frac{\xi t \sin t}{2} \tag{1.25}$$

$$x_{1,p3} = \left(\frac{\xi^2 - \varphi^2}{4} - 1\right) \frac{\xi \cos 3t}{8} \tag{1.26}$$

$$x_{1,p4} = \left(\frac{3\xi^2 - \varphi^2}{4}\right) \frac{\varphi \sin 3t}{8}. \tag{1.27}$$

After applying the initial conditions, $x_1(0) = 0$ and $\dot{x}_1 = 0$, the solution of $x_1(t)$ with homogeneous and particular terms can be derived as,

$$\begin{aligned} x_1(t) &= x_{1,h} + x_{1,p1} + x_{1,p2} + x_{1,p3} + x_{1,p4} \\ &= \left(4 - \xi^2 + \varphi^2\right) \frac{\xi \cos t}{32} - \left(16 + 5\xi^2 - 7\varphi^2\right) \frac{\varphi \sin t}{32} \\ &\quad + \left(1 - \frac{\varphi^2 + \xi^2}{4}\right) \frac{\varphi t \cos t}{2} + \left(1 + \frac{\varphi^2 - \xi^2}{4}\right) \frac{\xi t \sin t}{2} \\ &\quad + \left(\frac{\xi^2 - \varphi^2}{4} - 1\right) \frac{\xi \cos 3t}{8} + \left(\frac{3\xi^2 - \varphi^2}{4}\right) \frac{\varphi \sin 3t}{8}. \end{aligned} \tag{1.28}$$

Then, the first-order-approximated perturbation solution with potential resonance is,

$$\begin{aligned} x(t) &= \varphi \cos t + \xi \sin t + \left(4 - \xi^2 + \varphi^2\right) \frac{\varepsilon\xi \cos t}{32} - \left(16 + 5\xi^2 - 7\varphi^2\right) \frac{\varepsilon\varphi \sin t}{32} \\ &\quad + \left(1 - \frac{\varphi^2 + \xi^2}{4}\right) \frac{\varepsilon\varphi t \cos t}{2} + \left(1 + \frac{\varphi^2 - \xi^2}{4}\right) \frac{\varepsilon\xi t \sin t}{2} \\ &\quad + \left(\frac{\xi^2 - \varphi^2}{4} - 1\right) \frac{\varepsilon\xi \cos 3t}{8} + \left(\frac{3\xi^2 - \varphi^2}{4}\right) \frac{\varepsilon\varphi \sin 3t}{8}. \end{aligned} \tag{1.29}$$

The resonant effect is observed in Figure 3. Comparing to the no resonance case, the limit cycle boundary increases dramatically. By solving Van der Pol equation using perturbation for first order approximation, it is realized that initial condition can affect the performance significantly. The start-up condition of an oscillator is discussed in the next chapter.

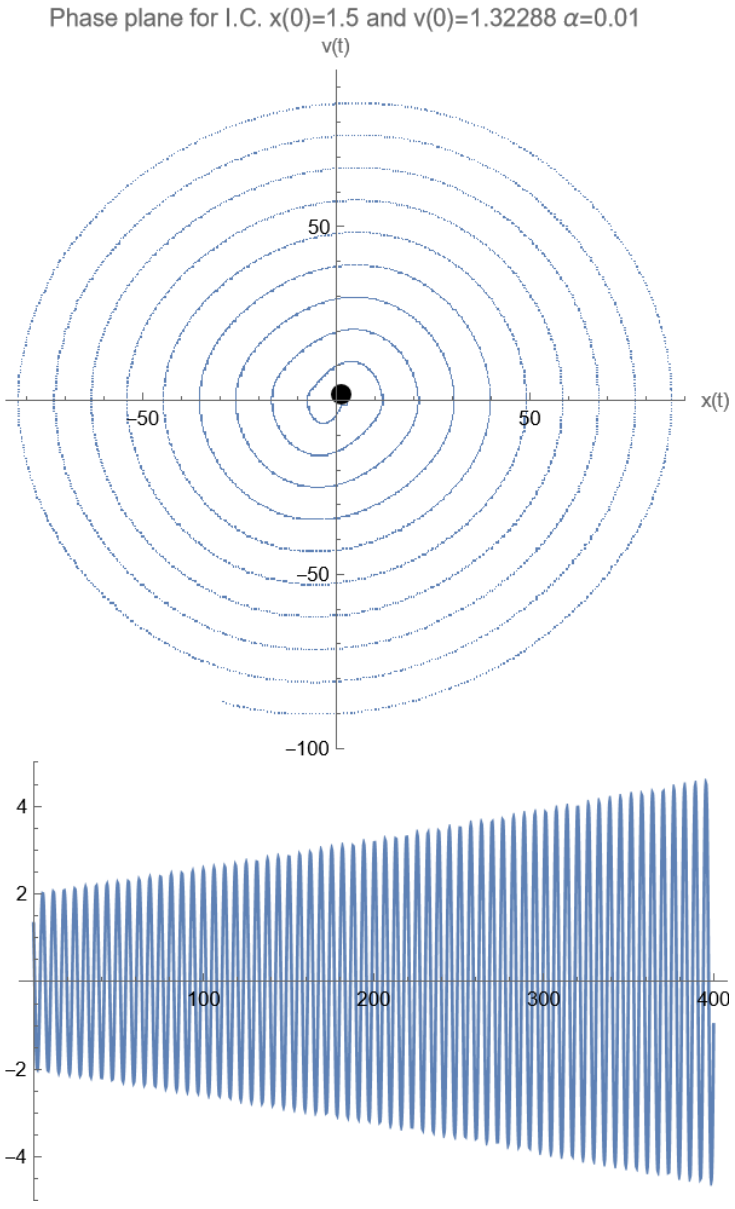

Figure 3. Resonance Case

1.2 Technologies Necessary to Construct a Nonlinear Phased Array

The rapid growth in bandwidth of wireless data links in recent years has led the industry towards utilizing range $24 - 60$ GHz for high-speed internet, data and voice channels and 77 GHz for automotive radar applications. The channel behavior has been studied and reported that antennas with appropriate characters can make the wireless channel very efficient and reliable. Intricate multi-antenna schemes such as MIMO and space-time coding can dramatically increase the channel throughput and frequency reuse. However, a full utilization of these benefits requires cost-effective implementations of the electronically scanning antenna (ESA) array architectures. Phased antenna array places important roles in the ESA system.

An ESA array must have two properties to be suitable for wide-band applications. First, the antenna elements and the feed network must be wide-band to allow proper matching and consistent array coefficients throughout the band. Second, the position of the main beam in the radiation pattern must be stable in the band of operation. A stable beam is necessary for systems with wide instantaneous bandwidth such as pulse communication or radars, or in fast orthogonal frequency division multiplexing (OFDM) type systems that the speed of electronic beam-steering can become limiting. A stable beam angle requires the use of true-time delay (TTD) devices to cancel the propagation delay differential from the antenna elements in a given direction at all frequencies. Simple phase-shifters can achieve this goal only at the design frequency. Figure 4 depicts the configuration of ESA arrays, in which ΔT is TTD or other type of phase shifter.

The phase shifters can be ferroelectric barium strontium titanate (BST) based

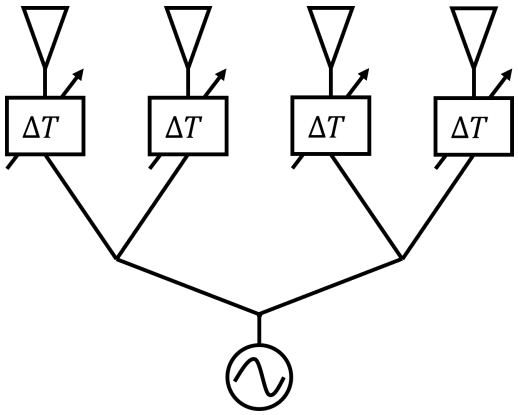

(a) Corporate Feed

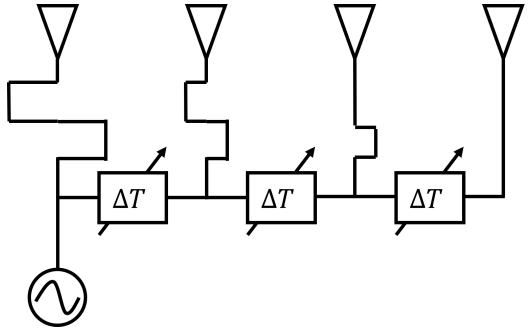

(b) True-Time Delay

Figure 4. Antenna Array with Phase Shifters

phase shifter of true-time delay, or CMOS devices, or MEMS products; either way they are cumbersome and costly. Table 1 provides a side to side comparison.

Metric Technology	MEMS	CMOS
Insertion Loss	$2-3$ dB	$6-8$ dB
Noise Figure	$2-3$ dB	> 4 dB
IIP3 (RX)	> 30 dBm	< -20 dBm
$P_{1-dB}(TX)$	> 15 dBm	~ 0 dBm
Operation Voltage	$20-80$ V	3.5 V
DC Consumption	~ 0 mW	10 mW
True-time Delay	Yes	No
Reciprocal	Yes	No

Table 1. A Side-By-Side Comparison of the Passive and Active Phase Shifters

Fortunately, the coupled phased array can provide antenna beam scanning electronically without TTD or any other phase shifters. The nonlinear dynamics show that for a coupled array of N elements satisfies [25]

$$\begin{aligned}
\frac{\mathrm{d}\theta_1}{\mathrm{d}t} &= \omega_1 - \frac{\omega_1\kappa}{2Q}\sin(\Phi+\theta_1-\theta_2),\\
\frac{\mathrm{d}\theta_i}{\mathrm{d}t} &= \omega_i - \frac{\omega_i\kappa}{2Q}\left[\sin(\Phi+\theta_i-\theta_{i-1})+\sin(\Phi+\theta_i-\theta_{i+1})\right], \quad 1<i<N\\
\frac{\mathrm{d}\theta_N}{\mathrm{d}t} &= \omega_N - \frac{\omega_N\kappa}{2Q}\sin(\Phi+\theta_N-\theta_{N-1}).
\end{aligned} \tag{1.30}$$

where θ_i is the instantaneous phase of each oscillator, ω_i is the free-running frequency of the ith oscillator, and Q is the quality factor of the oscillator elements, and $\kappa e^{j\Phi}$ is the coupling factor between adjacent oscillators. The steady state solution indicates that each oscillator has very close resonant frequencies and the small differences achieve the amount would be produced by the individual phase shifters.

Chapter 2

DESIGN OF THE OSCILLATOR ARRAY

In this chapter, a reliable coupled phased array to feed the scanning antenna array as a platform is studied [26, 27]. The coupled oscillators array (COA) regime is the framework for the application of Lyapunov theory to prevent unwanted defects such as Hopf bifurcation, quasi-periodic route to chaos, and exponential divergence. We have studied Lyapunov stability, limit cycles, bifurcation, and phase locking principles, and then moved on to resonator and antenna design.

We apply the Van der Pol model to a single-transistor oscillator (STO) and obtain the isolated limit cycle. Employing the Keysight ADS, we tune and optimize the STO with a free-running frequency $f_s = 5.35$ GHz. The STO circuit and its mirror image are joined by a Wilkinson power combiner, forming a double-transistor oscillator (DTO) that is a frequency doubler (see Figure 12), with the second harmonic as output, namely, a free-running frequency $f_d = 10.71$ GHz. Throughout the paper, the antenna operating frequency is $f_d = 10.71$ GHz, while the oscillator free running frequency is $f_s = 5.35$ GHz. In such a configuration, the antenna scanning range will be augmented remarkably.

An example of a voltage-controlled oscillator (VCO) from the ADS design library is studied for the varactor design and implementation. The results show a linear variation of the resonant frequency when adjusting the tuning voltage. The varactor is then applied to the project for setting up a resonant frequency configuration of the phased array.

The output performance of the phased oscillator array is investigated. The phase

and amplitude relationships between neighboring elements in differential equation form are derived from Adler's equation. The equations are solved numerically using the Runge-Kutta method. The results are compared with the simulation results from the ADS model.

2.1 Single-Transistor Oscillator Design

Self-oscillating circuit is the basic unit for coupled COA systems. We conducted design and simulation of self-oscillating circuits using Keysight PathWave Advanced Design System (ADS). Resonator and oscillator theory and practice are in the literature and college textbooks. Based on piezoelectric resonance, crystal oscillators are stable and precise operating in the low mega-hertz region. Hartley-Colpitts oscillators are types of feedback networks, work in the mega-hertz and sub-GHz region. Transistor oscillators generally have lower frequency and power capabilities than diode sources but more flexible and compatible with monolithic microwave integrated circuit (MMIC), and we choose to use transistors. Dielectric resonator and split ring resonator (SRR) may provide oscillations in the X- to Ku- band, but they require specific components. In our design, we use gate stub resonance, employing only microstrip transmission lines without high-Q disk or SRR.

2.1.1 Circuit and Component Selection

Among BJT and FET, the BJT usually has slightly higher frequency and uses more current. We selected the NEC's NE3201S01, which is a low noise AlGaAs/InGaAs

N-channel pseudomorphic Hetero-Junction FET with $f_c = 12$ GHz. Table 2 below lists its electric characteristics at temperature $T = 25°$ C.

Characteristics	Symbol	Test Conditions	MIN	TYP	MAX	Unit
Gate to Source Leak Current	I_{GSO}	$V_{GS} = -3V$	–	0.5	10	μA
Saturated Drain Current	I_{DSS}	$V_{DS} = 2V$, $V_{GS} = 0V$	15	40	70	mA
Gate to Source Cut-Off Voltage	$V_{GS(off)}$	$V_{DS} = 2V$, $I_{DS} = 10mA$	-0.2	-0.7	-2.0	V
Transconductance	g_m	$V_{DS} = 2V$, $I_{DS} = 10mA$	40	55	–	mS
Noise Figure	NF	$V_{DS} = 2V$, $I_{DS} = 10mA$, $f = 12GHz$	–	0.35	0.45	dB
Associated Gain	G_a	$V_{DS} = 2V$, $I_{DS} = 10mA$, $f = 12GHz$	12.0	13.5	–	dB

Table 2. Electric Characteristics of NE3201S01

This FET model is within the ADS libraries provided by Renesas Electronics Corporation [28] and readily for simulation. The device, NE3201S01 is obsolete and its drop-in replacement is CEL's CE3512K2.

Based on NE3201S01 data sheet and S-parameters, we conducted the stability $\mu' - \mu$ test that the device will be working in the unstable condition around $f = 5.4$ GHz. Figure 8 depicts the ADS schematic and the simulation results.

Figure 8 illustrates the DC bias circuit. Under 4 volts dc voltage the drain current is close to the typical values of Table 2, namely $V_{DS} = 2V, I_{DS} = 10mA$.

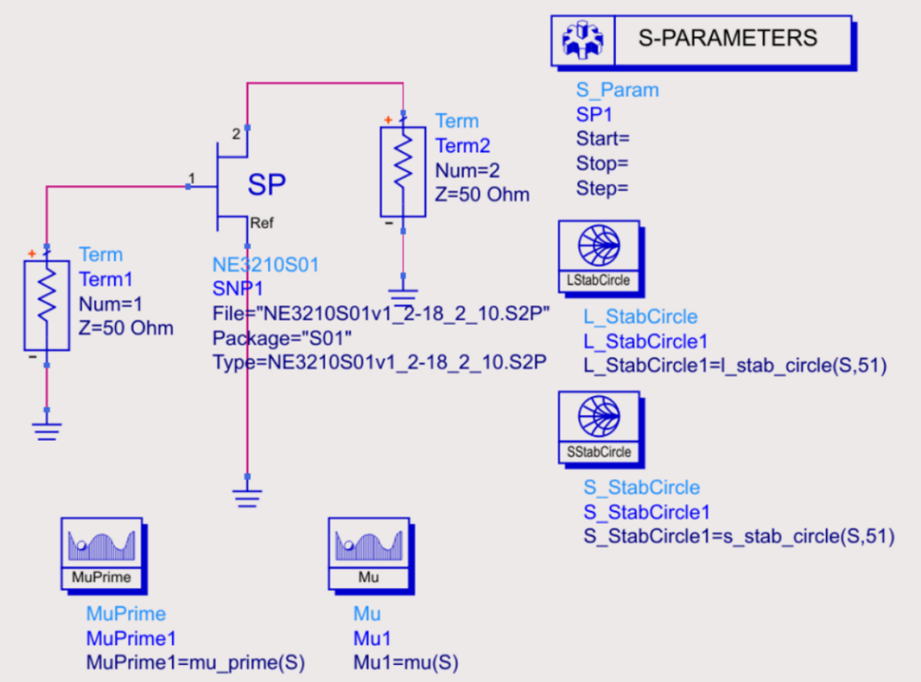

Figure 5. Stability Tests and Schematic

freq	Mu1	MuPrime1
5.400 GHz	0.912	0.732

Figure 6. Stability Values, μ and μ'

2.1.2 Single Transistor Oscillator Based upon Gate Stub Resonator

The resonating mechanism of single transistor oscillator is negative resistance, or equivalently negative total admittance, namely,

$$\mathbf{Re}\left\{Y_T\right\}_{\omega=\omega_0} < 0 \tag{2.1}$$

The Kurokawa resonation criteria require admittance crossing zero at resonant frequency,

$$\mathbf{Im}\left\{Y_T\right\}_{\omega=\omega_0} = 0 \tag{2.2}$$

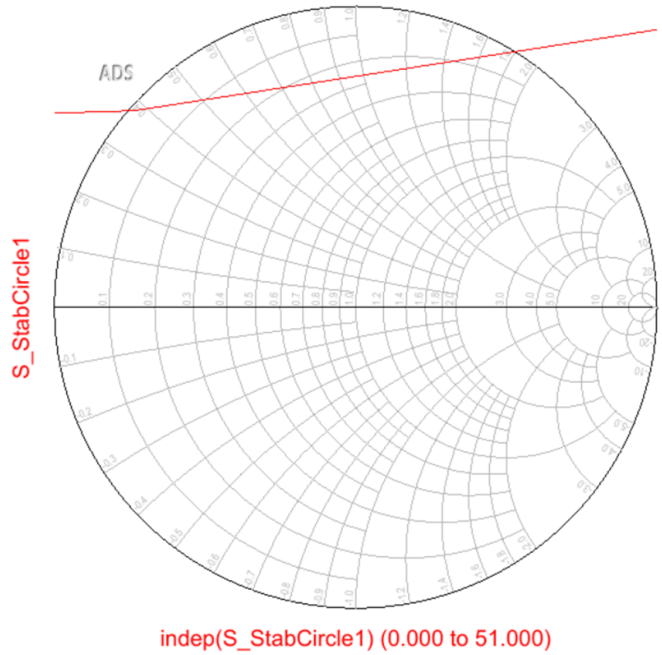

(a) Source Circle

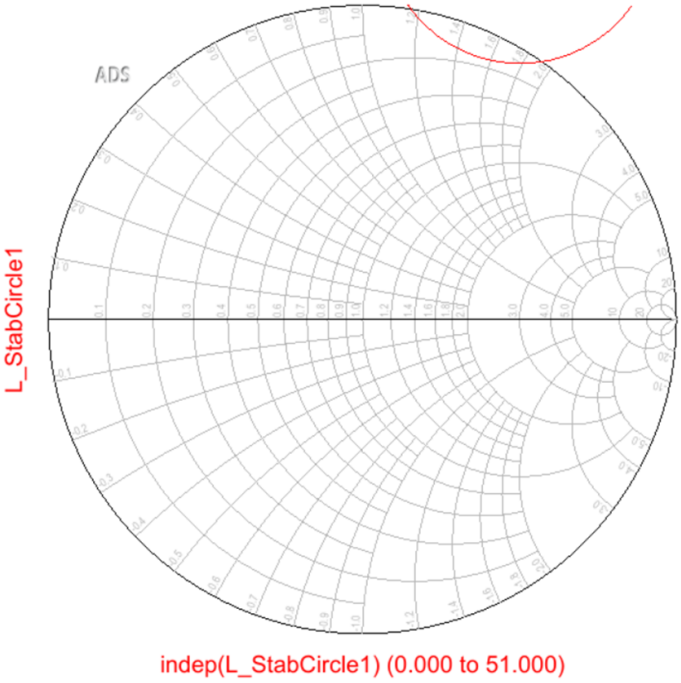

(b) Load Circle

Figure 7. Stability Circles

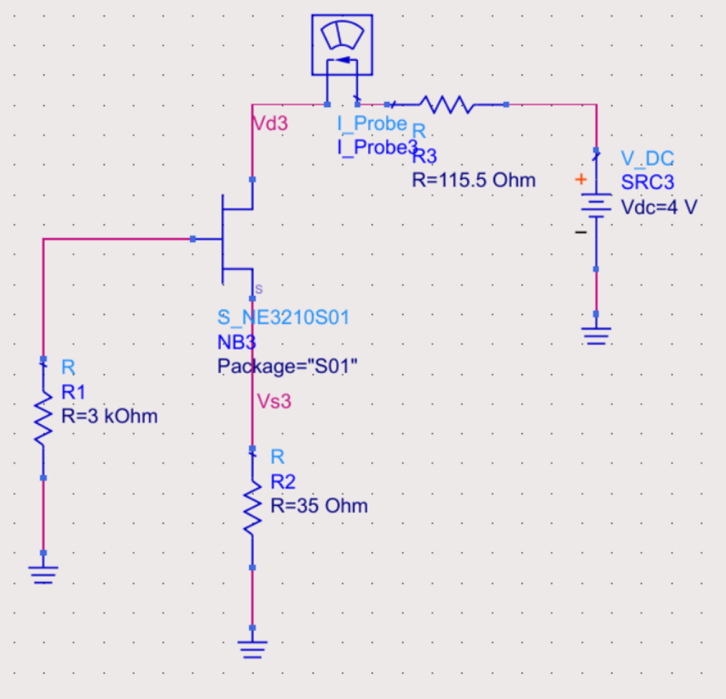

freq	Vd3-Vs3	I_Probe3.i	Vd3	Vs3
0.0000 Hz	1.992	13.35 mA	2.459 V	467.1 mV

Figure 8. DC Bias Circuit and Typical Drain-Source Conditions

and

$$\frac{\partial \mathbf{Im}\left\{Y_T\right\}_{\omega=\omega_0}}{\partial \omega}|_{\omega=\omega_0} > 0 \tag{2.3}$$

Equations above are the start-up conditions. For gate stub resonator, we first choose source stub width to match the device source pad, and the line impedance per unit length is determined by the substrate selected. The length is such that the negative resistance is preserved in the frequency sub-bands.

The transmission lines and stub by drain-gate are to convert negative resistance to network 50Ω environment. Figure 9 demonstrates the ADS schematic diagram of a single FET self-oscillator whose 1^{st} harmonic is 5.35 GHz.

Figure 10 shows the time-domain waveform of this single FET self-oscillator. Its

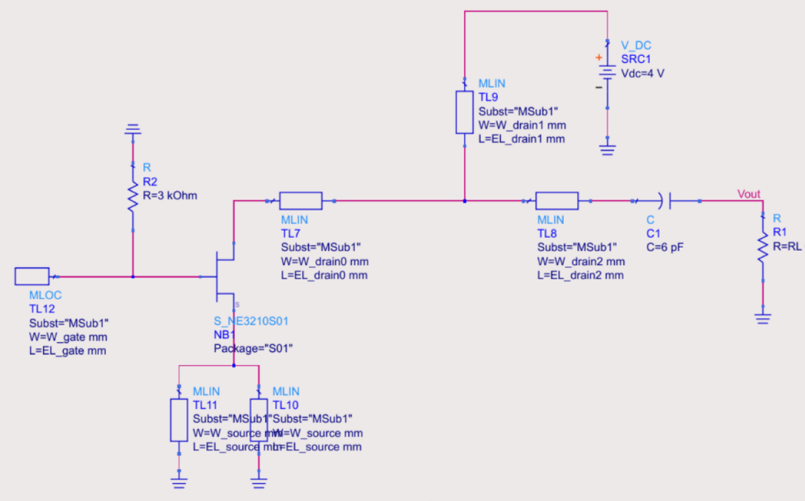

Figure 9. ADS Schematic Diagram of Single FET Self-Oscillator with $f = 5$ GHz

start-up, transient and steady state stages are clearly observed. The frequency-domain discrete Fourier transform of the waveform shows the fundamental frequency $f_1 = 5.35$ GHz, and output power in 9.42 dBm, and 2^{nd} harmonic $f_2 = 10.71$ GHz, and output power in -1.65 dBm.

Figure 11 shows the validation of the design principles. Negative resistance preserved at the resonant frequency, and the slop of imaginary part of the admittance is upward.

2.2 Push-Pull Transistor Oscillator Design

On many occasions, higher frequencies are desired. If we combine two identical single transistor oscillators with a Wilkins power combiner, we may cancel the odd harmonics and enhance the even harmonics by connecting a series of transmission

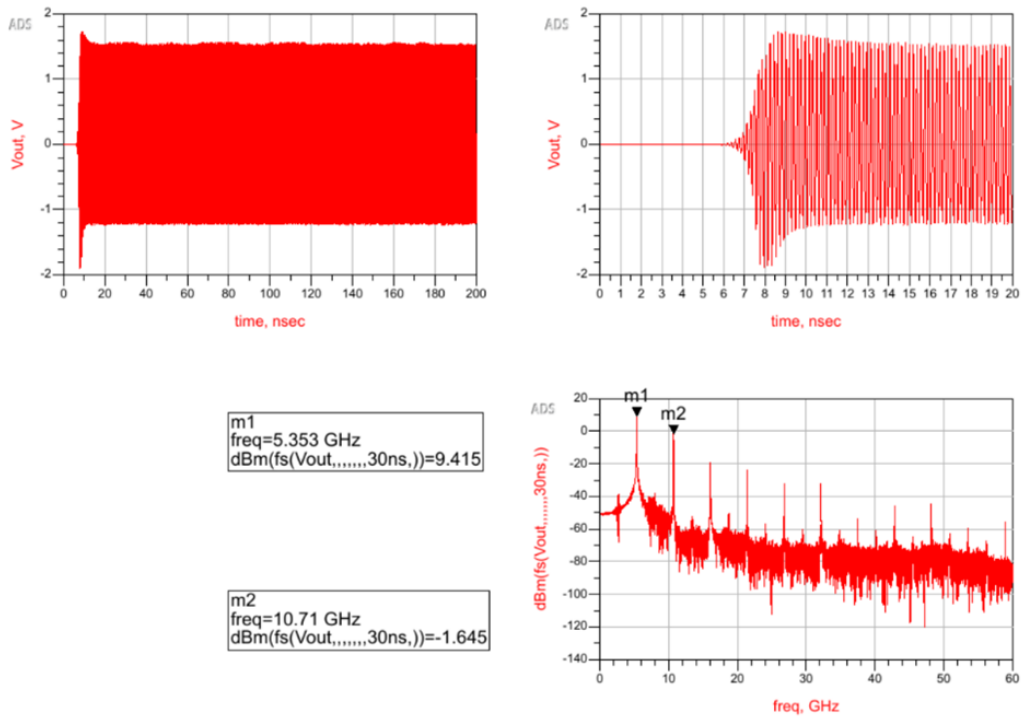

Figure 10. Performance of the Single FET Self-Oscillator in Time and Frequency Domains

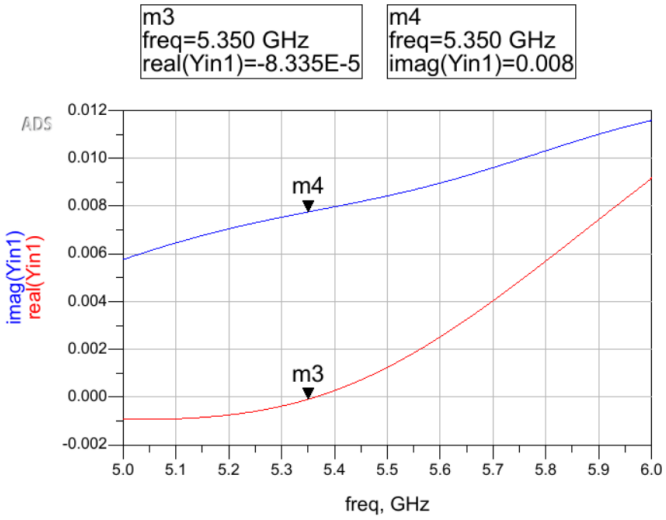

Figure 11. Start-Up Condition Verification for the Single FET Self-Oscillator

lines between the gates of the FET devices. As a result, the push-pull oscillator is designed. Figure 12 is the ADS schematic.

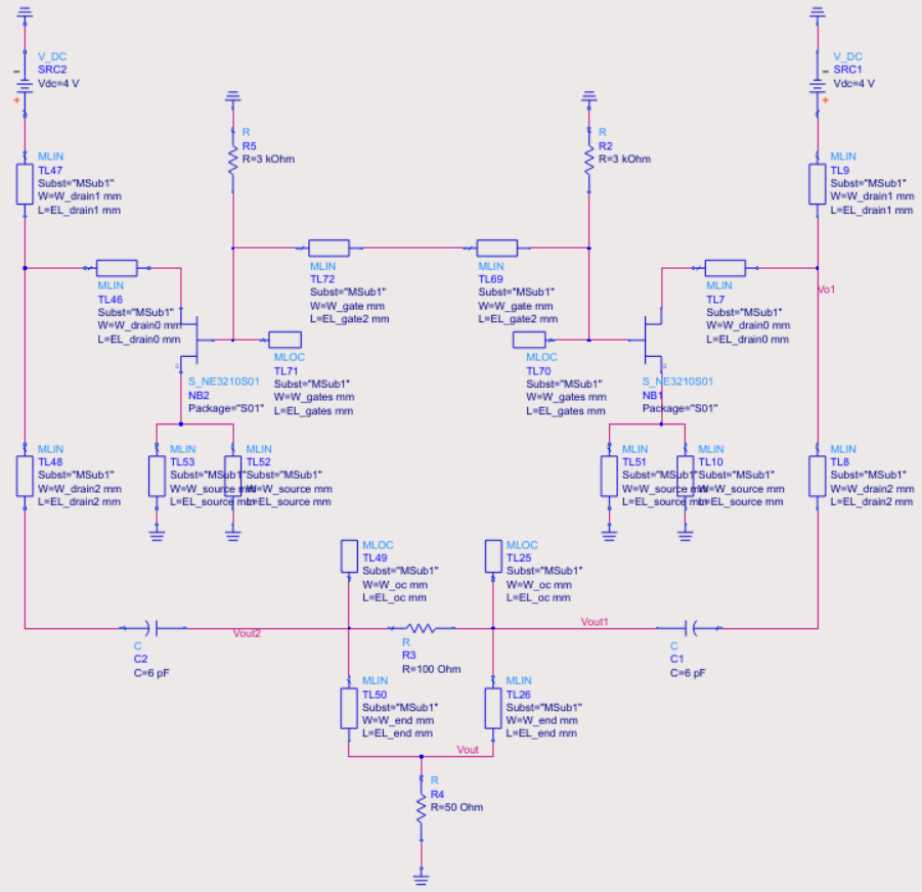

Figure 12. ADS Schematic Diagram of Push-Pull FET Self-Oscillator at Second Harmonic Frequency

Figure 13 and Figure 14 show the simulation results of the push-pull oscillator. The best resonating frequency appears to be at 10.3 GHz, at which all three criteria are satisfied. The analysis of time-domain results indicates that the ultimate resonant frequency is 10.82 GHz. The output power is 0.539 dBm, which is improved by 2.1 dB compared to the 2^{nd} harmonic power of the single FET oscillator. Further study and work are needed to fully understand the nonlinear oscillator.

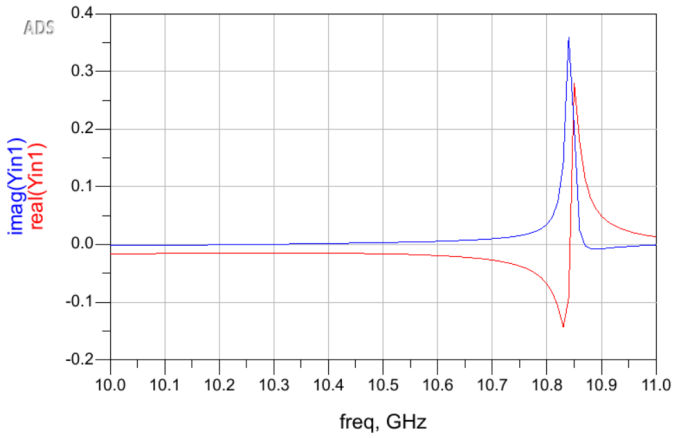

Figure 13. Start-Up Condition Verification for Push-Pull Oscillator

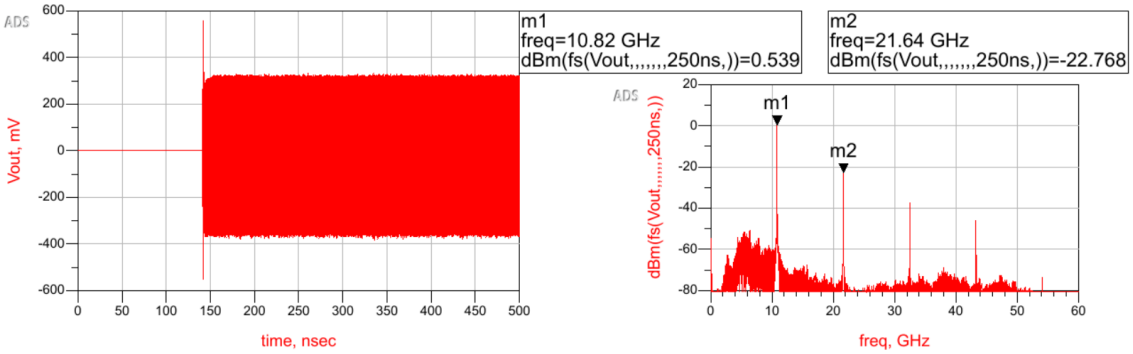

Figure 14. Performance of the Push-Pull FET Oscillator in Time and Frequency Domains

2.3 Voltage-Controlled Oscillator

The topology of single FET oscillator of Figure 9 and double FET push-pull oscillator of Figure 12 is easily to control. Figure 15 is the schematic of an open loop resonance model for NEC 3210S01 HJFET based voltage-controlled oscillator (VCO),

where a varactor, C_{var}, is connected to the gate of the FET. By changing the voltage of C_{var} and associated transmission line parameters, the resonant frequency can be tuned and optimized.

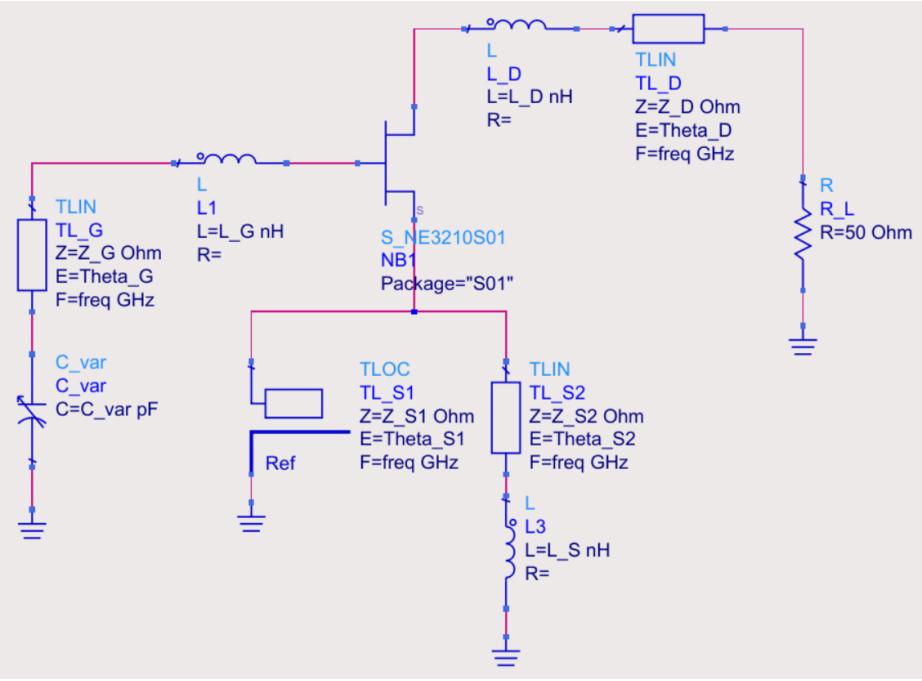

Figure 15. Schematic of Open Loop Resonance Model

The adjustable capacitor, varactor, near the gate stub can be achieved with a FET or diode. Figure 16 is an example from the help document of ADS shows the testing and integration procedures of designing a varactor.

Figure 16 shows a biased FET being tested as a varactor. The linearity of voltage change can be observed in the figure, and this phenomenon will be utilized to adjust the resonant frequency.

Figure 17 demonstrates a VCO design with an FET used as a varactor. The resonant frequency varies by more than 250 MHz as the tuning voltage changes from

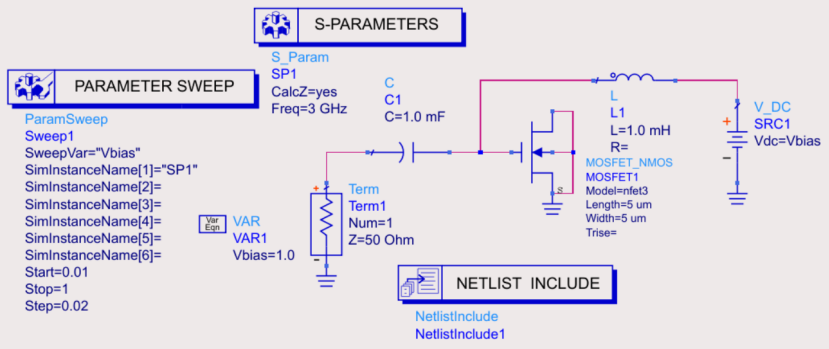

(a) Varactor Testing Circuit

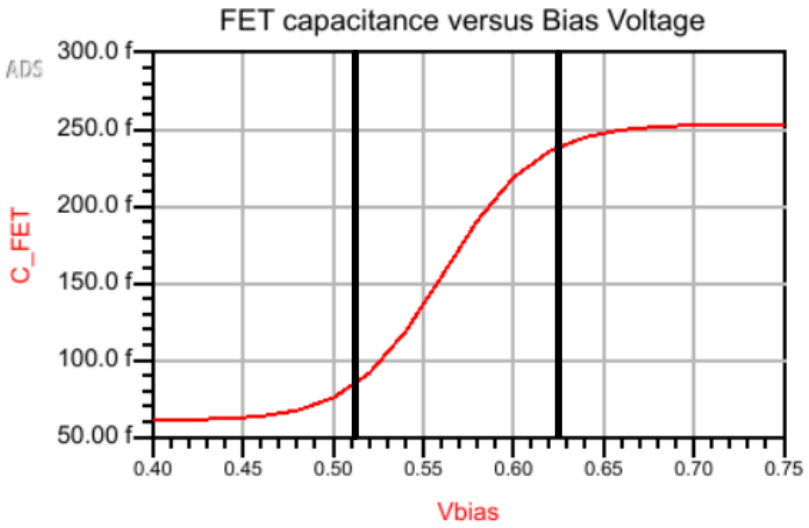

(b) Capacitance with Control Voltage (Linear Part Marked)

Figure 16. Voltage Variation of a Biased FET for Varactor Designing

2.8 V to 3.3 V. However, the slope of the frequency differential rate is not constant, which increases the complexity of controlling the phased oscillator array.

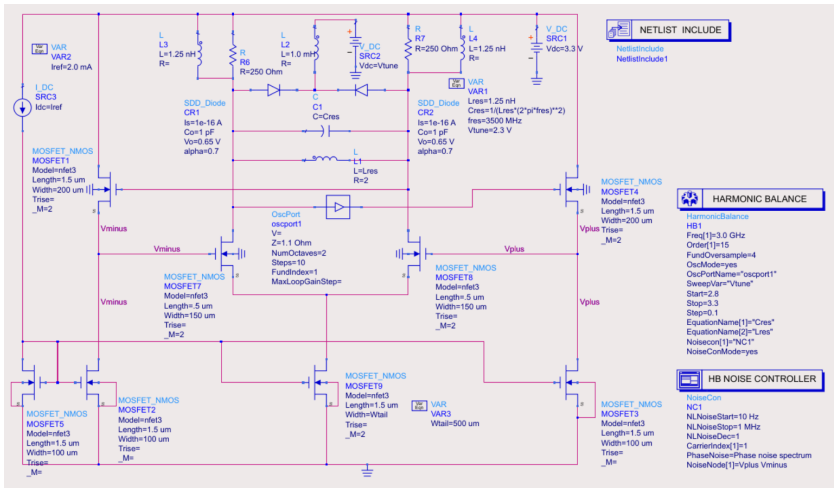

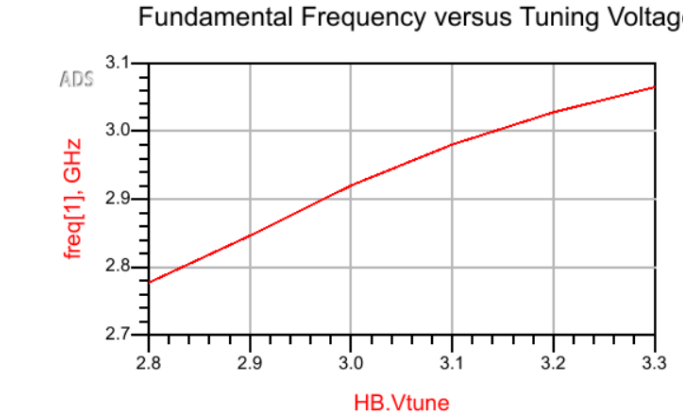

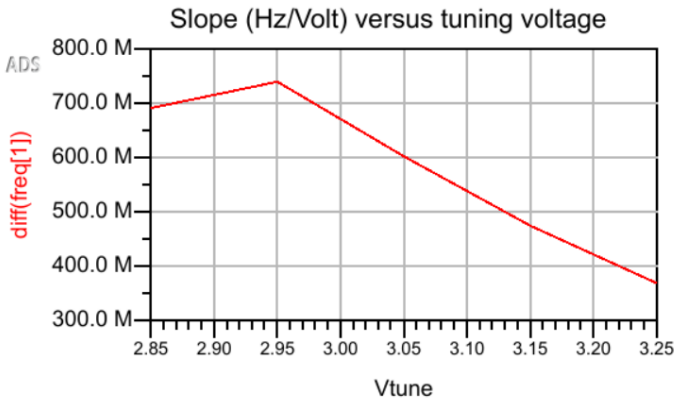

Figure 17. An ADS Example of VCO with Varactor Operating at 3 GHz

2.4 Phased Oscillator Array

2.4.1 Phase Relationship Derived from Adler's Equation

The output phase of an oscillator with an injected signal is given by Adler's equation:

$$\frac{\mathrm{d}\phi}{\mathrm{d}t} = \omega_0 - \omega_{inj} + \frac{\rho\omega_0}{2\alpha Q}\sin(\psi - \phi), \tag{2.4}$$

where ω_0 is the free-running frequency, α is the amplitude of the free-running output, and Q is the quality factor of the resonant circuit, ρ, ω_{inj} and ψ are the amplitude, frequency and phase of the injected signal respectively. The "locking range" is defined as,

$$\Delta\omega_m = \frac{\rho\omega_0}{2\alpha Q}. \tag{2.5}$$

For the steady-state, $\frac{\mathrm{d}\phi}{\mathrm{d}t} = 0$, relationship between the phase and the instantaneous frequency is derived as

$$\frac{\omega - \omega_0}{\Delta\omega_m} = \sin(\psi - \phi). \tag{2.6}$$

By solving the steady-state, phase difference between the oscillator and injected signal is,

$$\Delta\phi = \sin^{-1}\left(\frac{\omega_{inj} - \omega_0}{\Delta\omega_m}\right). \tag{2.7}$$

Equation 2.7 indicates that the frequency difference between injected signal and oscillator must be within the locking range for a valid injection-locked solution.

The steady-state phase is perturbed from its free-running state, $\phi = \phi_0 + \phi_\delta$, Equation 2.4 and be reduce to

$$\frac{\mathrm{d}\phi_\delta}{\mathrm{d}t} = -\phi_\delta\Delta\omega_m\cos(\Delta\phi). \tag{2.8}$$

The criteria for the perturbation decays in time, $\frac{\mathrm{d}\phi_\delta}{\mathrm{d}t} < 0$, is $\cos\Delta\phi > 0$. Thus, the phase range is restricted:

$$-\frac{\pi}{2} < \Delta\phi < \frac{\pi}{2}. \tag{2.9}$$

Since the Q factor is known as frequency-to-bandwidth ratio, Equation 2.5 can be rewritten as

$$\begin{aligned}\Delta\omega_m &= \frac{\rho\omega_0}{2\alpha Q} = \frac{\rho\omega_0}{2\alpha}\frac{\Delta\omega_{3dB}}{\omega_0} = \frac{\rho}{2\alpha}\Delta\omega_{3dB},\\ \Delta f_m &= \frac{\rho}{2\alpha} f_{3dB}.\end{aligned} \tag{2.10}$$

To enlarge the locking range in a practical design, the designer could increase the injection-oscillator amplitude ratio, or increase the resonant frequency. Thus, the coupled phased array can provide antenna beam scanning electronically without TTD or any other phase shifters.

For one-dimensional nearest-neighbor coupled oscillator array,

$$Y_i(\omega,[V]) = Y_{OSC,i}(\omega,V_i) + Y_{CPL,i}(\omega,[V]) = 0, \quad i = 1,2,\cdots,N \tag{2.11}$$

$$Y_{CPL,i} = \sum_{j=1}^{N} Y_{ij}\frac{V_j}{V_i} \tag{2.12}$$

$$Y_{ij} = y_{ij}e^{-j\Phi_{ij}} \tag{2.13}$$

where y_{ij} is the coupling strength, and Φ_{ij} is the coupling phase between oscillator i and j.

$$V_i = A_i(t)e^{j\theta_i(t)} \tag{2.14}$$

where A_i and θ_i are the amplitude and the instantaneous phase of the ith oscillator.

The input admittance of a shunt equivalence showing in Figure 18 is written as:

$$Y_{OSC}(\omega,V_i) = \frac{1}{j\omega L} - G_d + G_L + j\omega C. \tag{2.15}$$

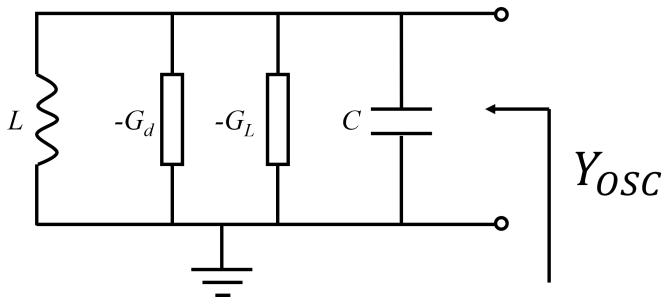

Figure 18. The Shunt-Resonance Equivalent Circuit of an Oscillator

And for a one-dimensional phased oscillator array, the admittance parameters can be derived as:

$$Y_{ij} = \begin{cases} \frac{1}{2Z_0}, & \text{if} \quad i = j = 1 \text{ or } N \\ \frac{1}{Z_0}, & \text{if} \quad i = j \neq 1 \text{ and } N \\ \frac{-1}{Z_0} e^{-j\Phi}, & \text{if} \quad |i - j| = 1 \\ 0. & \text{otherwise} \end{cases} \tag{2.16}$$

The nonlinear dynamics show that for a coupled array of N elements satisfies [25]

$$\begin{aligned} \frac{\mathrm{d}\theta_1}{\mathrm{d}t} &= \omega_1 - \frac{\omega_1 \kappa}{2Q} \sin(\Phi + \theta_1 - \theta_2), \\ \frac{\mathrm{d}\theta_i}{\mathrm{d}t} &= \omega_i - \frac{\omega_i \kappa}{2Q} \left[\sin(\Phi + \theta_i - \theta_{i-1}) + \sin(\Phi + \theta_i - \theta_{i+1})\right], \quad 1 < i < N \\ \frac{\mathrm{d}\theta_N}{\mathrm{d}t} &= \omega_N - \frac{\omega_N \kappa}{2Q} \sin(\Phi + \theta_N - \theta_{N-1}), \end{aligned} \tag{2.17}$$

and

$$\begin{aligned} \frac{\mathrm{d}A_1}{\mathrm{d}t} &= \frac{\omega_1 A_1}{2Q} \left[\mu S_1(A_1) - \kappa \cos\Phi\right] + \frac{\omega_1 \kappa}{2Q} A_2 \cos(\Phi + \theta_1 - \theta_2), \\ \frac{\mathrm{d}A_i}{\mathrm{d}t} &= \frac{\omega_i A_i}{2Q} \left[\mu S_i(A_i) - 2\kappa \cos\Phi\right] \\ &\quad + \frac{\omega_i \kappa}{2Q} \left[A_{i-1} \cos(\Phi + \theta_i - \theta_{i-1}) + A_{i+1} \cos(\Phi + \theta_i - \theta_{i+1})\right], \\ \frac{\mathrm{d}A_N}{\mathrm{d}t} &= \frac{\omega_N A_N}{2Q} \left[\mu S_N(A_N) - \kappa \cos\Phi\right] + \frac{\omega_N \kappa}{2Q} A_{N-1} \cos(\Phi + \theta_N - \theta_{N-1}), \end{aligned} \tag{2.18}$$

where θ_i is the instantaneous phase of each oscillator, ω_i is the free-running frequency of the ith oscillator, and Q is the quality factor of the oscillator elements, and $\kappa e^{j\Phi}$ is the coupling factor between adjacent oscillators.

$$\kappa = \frac{y_{ij}}{G_L} = \frac{1}{2Z_0 G_L} \tag{2.19}$$

The steady state solution indicates that each oscillator has very close resonant frequencies and the small differences achieve the amount would be produced by the individual phase shifters.

The steady-state phase shift $(\theta_i - \theta_{i+1})$ can be obtained as:

$$\theta_i - \theta_{i+1} = \arcsin\left[\frac{1}{\rho}\left(\sum_{k=1}^{i}\omega_k - \frac{i}{N}\sum_{i=1}^{N}\omega_i\right)\right]. \tag{2.20}$$

A coupled oscillator array configuration addressed in [10] that the oscillators' resonant frequency at the boundaries are tuned away from other middle elements by $\Delta\omega$ and $-\Delta\omega$. The linear inter-element shift is calculated as:

$$\begin{aligned}\theta_i - \theta_{i+1} &= \arcsin\left[\frac{1}{\rho}\left(\sum_{k=1}^{i}\omega_k - \frac{i}{N}\sum_{i=1}^{N}\omega_i\right)\right] \\ &= \arcsin\left[\frac{1}{\rho}\left(\bar{\omega} + \Delta\omega + \sum_{k=2}^{i}\omega_k - \bar{\omega}i\right)\right] \\ &= \arcsin\left(\frac{\Delta\omega}{\rho}\right).\end{aligned} \tag{2.21}$$

2.4.2 Evaluate Phase Shifts with Different Methods

The dynamic behavior of the locking process can be analysed by numerically solving Equation 2.18. The Runge–Kutta method is adopted for iteratively evaluate the output phases from each coupled oscillator. A MATLAB script in Appendix is developed according to:

$$y_{n+1} = y_n + \frac{1}{6}(k_1 + 2k_2 + 2k_3 + k_4)h, \tag{2.22}$$

where

$$\begin{cases} t_{n+1} = t_n + h, \\ k_1 = f(t_n, y_n), \\ k_2 = f(t_n + \frac{h}{2}, y_n + h\frac{k_1}{2}), \\ k_3 = f(t_n + \frac{h}{2}, y_n + h\frac{k_2}{2}), \\ k_4 = f(t_n + h, y_n + hk_3). \end{cases}$$

With the estimated values, $\kappa = 0.8$, $Q = 3.8$, $\Delta\omega = 100$MHz, and $\omega = 5.3$ GHz, the results of different initial conditions converge to the the same phase shift value, shown in Figure 19.

In order to verify the results obtained using the Runge-Kutta method, a simulation model is built in ADS with the same resonant frequency configuration. Figure 20 shows the schematic of the phased array, and Figure 21 demonstrates evenly separated oscillator outputs with the expected phase shift. Comparing the results from the Runge-Kutta method and ADS simulation, as shown in Figure 22, they show good agreement in terms of the linearity of the phase distribution.

In Figure 23, the outputs of all the oscillators in the time domain and frequency domain are plotted. It shows that the resonant frequency of all oscillators is synchronized at 5.3 GHz, although the two on the boundaries are resonating at 5.4 GHz and 5.2 GHz, respectively.

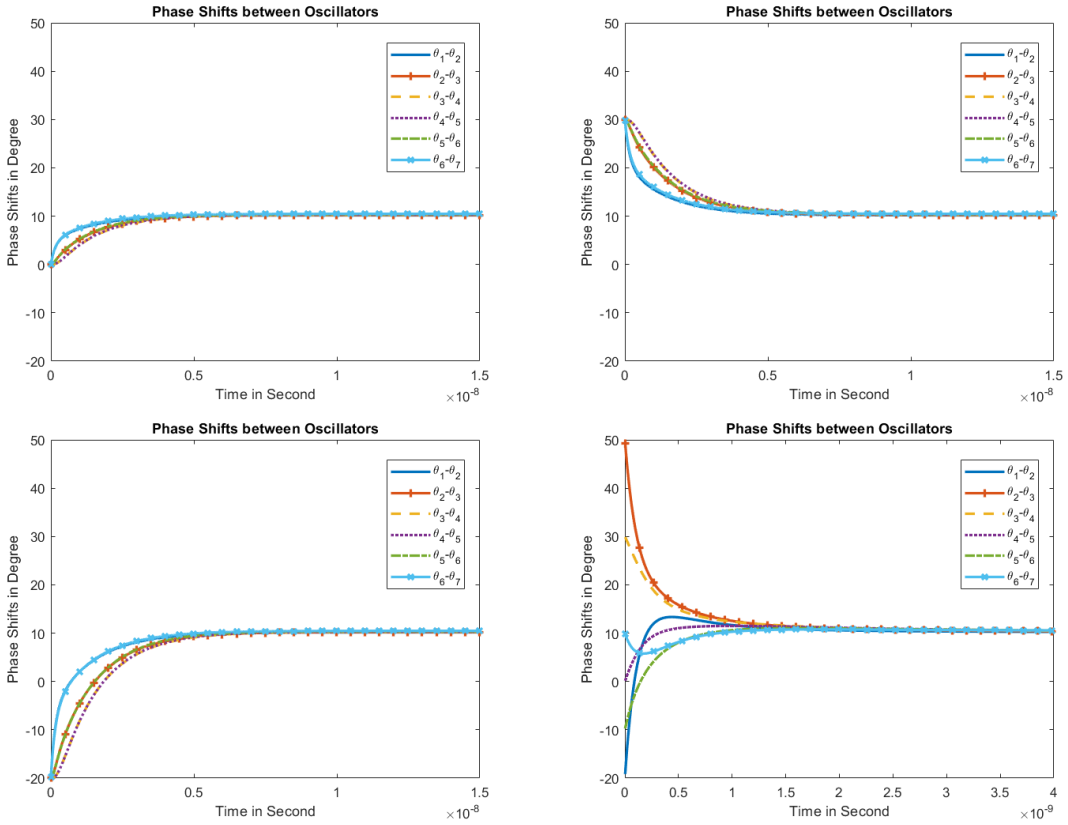

Figure 19. Solving the Phase Shifts between Neighbor Oscillators with the Runge-Kutta Method

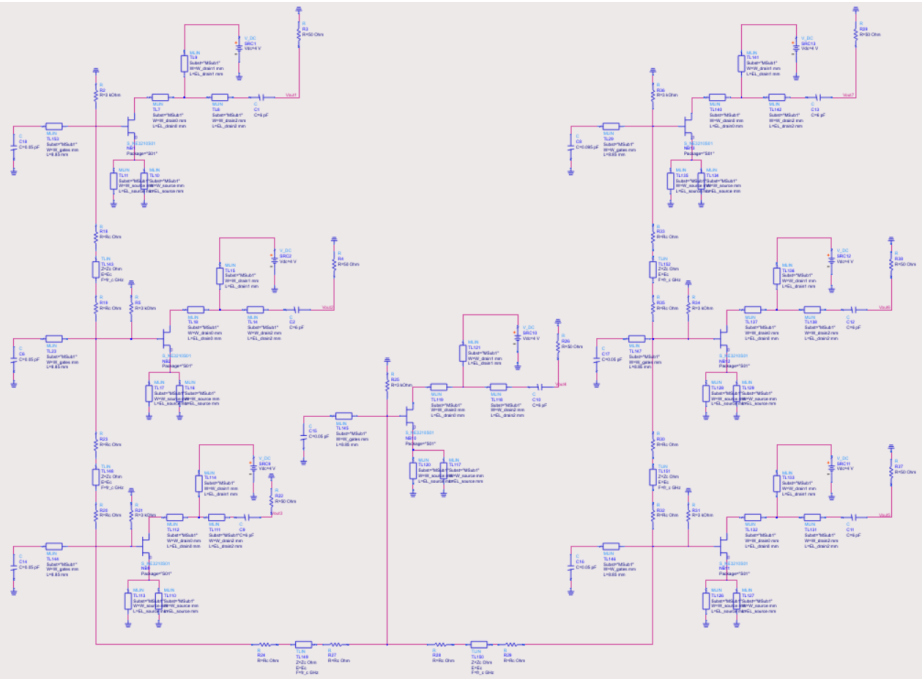

Figure 20. Bilateral Coupling Configuration of the Phased Oscillators.

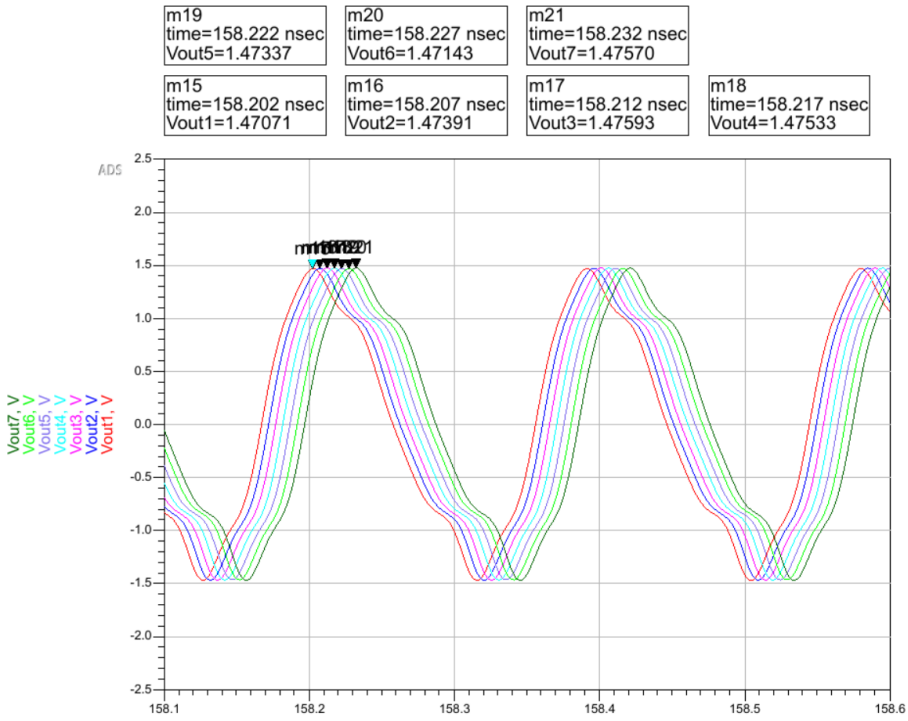

Figure 21. Time-Domain Result from ADS that Shows the Phase Shifts between Each Oscillator

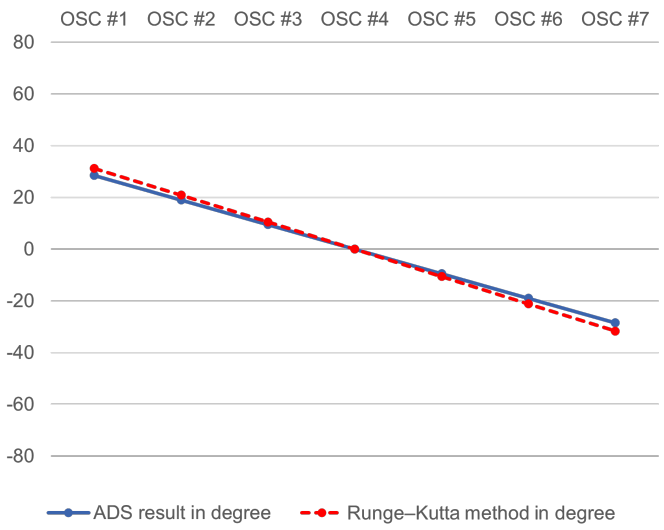

Figure 22. Plot of Output Phases from ADS Simulation and the Runge-Kutta Method

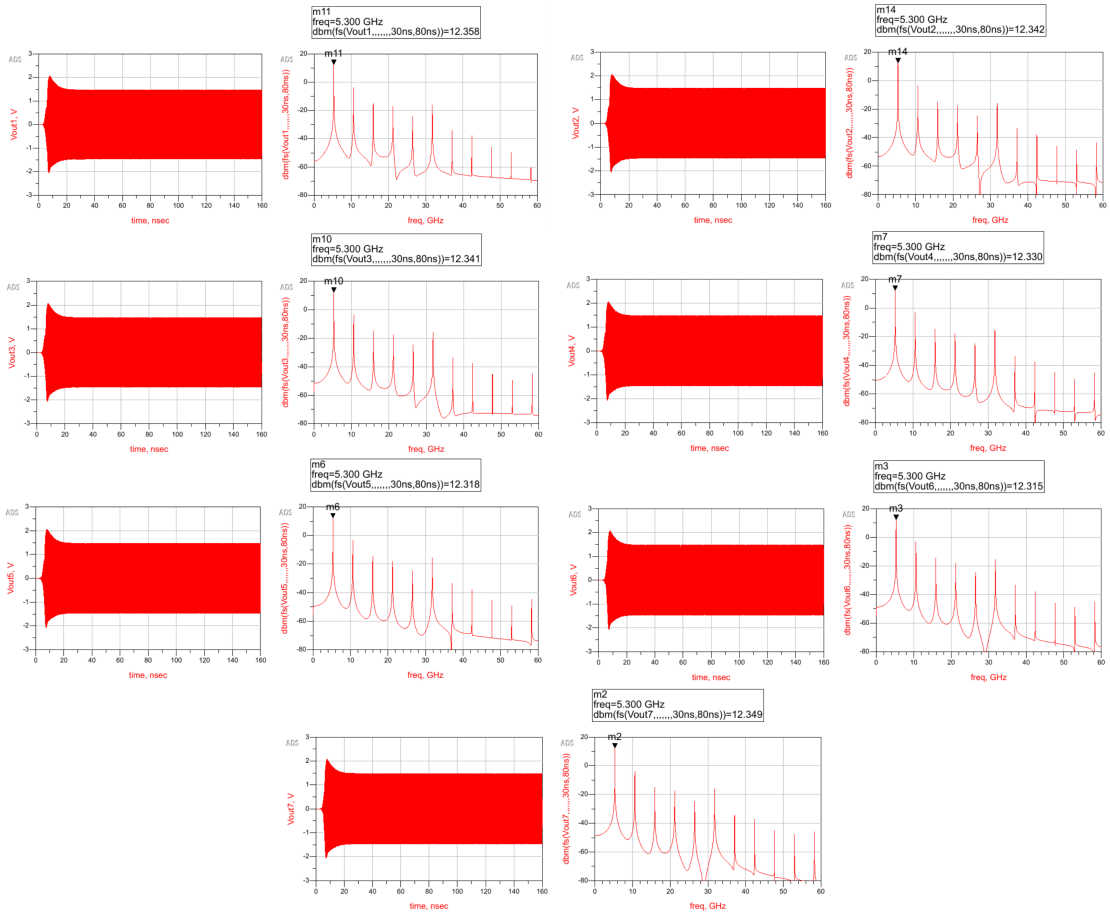

Figure 23. Oscillator Outputs in Time Domain and Frequency Domain from ADS Simulation

Chapter 3

ANTENNA ELEMENTS OPTIMIZATION AND ARRAY DESIGN

In this chapter, three types of antennas are studied and implemented in a simulation software, Ansys HFSS. Section 3.1 presents the optimization of the feeding of horn antennas and their cross-coupling. Section 3.2 discusses impedance matching of a cavity-backed slotted antenna. The gain improvement of a cavity slotted array is shown in Section 3.3. Section 3.4 demonstrates a uniform antenna array with coupled oscillators implemented.

3.1 Optimization of Feeding of Horn Antennas and Cross Coupling

The horn antenna is studied due to its characteristics of high gain and low cross-talk. These advantages make the horn antenna a good candidate for automobiles. However, the disadvantage of horn antennas is their high profile. Unlike cavity-backed slotted antennas that can be made on a printed circuit board (PCB), horn antennas occupy more space and their scale is positively correlated to the operating wavelength. A pyramidal horn antenna working at 76.5 GHz, designed in HFSS, is shown in Figure 24.

The simple design in Figure 24 meets the requirement of gain by using the default feeding port provided by HFSS, which assumes the antenna is fed by a rectangular waveguide. Waveguide provides low attenuation. However, feeding by a waveguide is not only hard to implement in circuits, but also requires more longitudinal space.

To overcome the disadvantage, an improved model, shown in Figure 25, fed by a

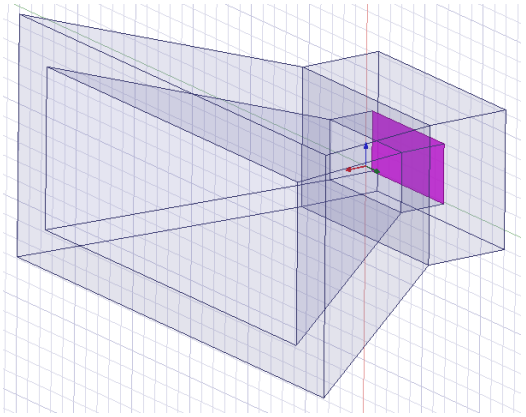

Figure 24. Pyramidal Horn Antenna in HFSS

coaxial cable is built. This design is able to be connected to a Sub-Miniature version A (SMA) adaptor. An optimization is essential to shrink the size of device and match the circuit.

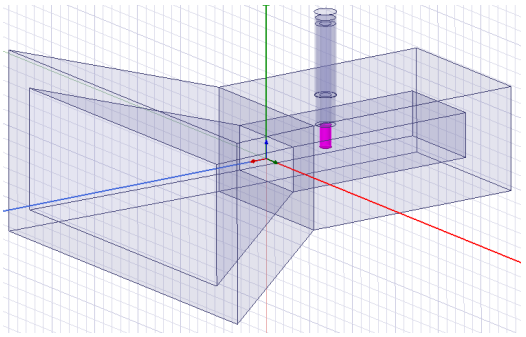

Figure 25. Pyramidal Horn Antenna Fed by Coaxial Cable

As indicated in Figure 26, the performance of the matching network is determined by three variables. d is the length of the probe part, l is the distance from the center of the probe to the back wall, and hw is the depth of the waveguide part.

The problem has been analysed in [29]. It mentioned the dimensions of coaxial aperture have a significant influence on the matching network. For this specific design,

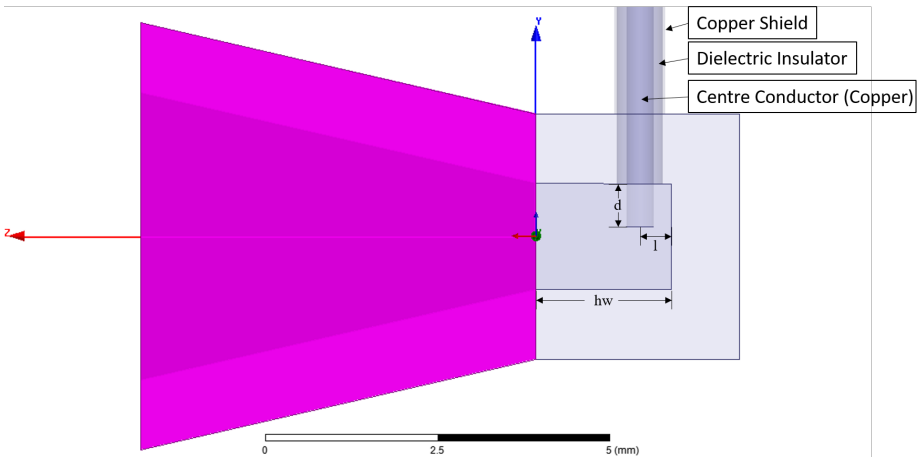

Figure 26. Feeding Network Variables (Side View)

variables are determined by optimization procedure. Thus, $d = 0.63$ mm, $l = 0.475$ mm and $hw = 2$ mm. The return loss is plotted in Figure 27.

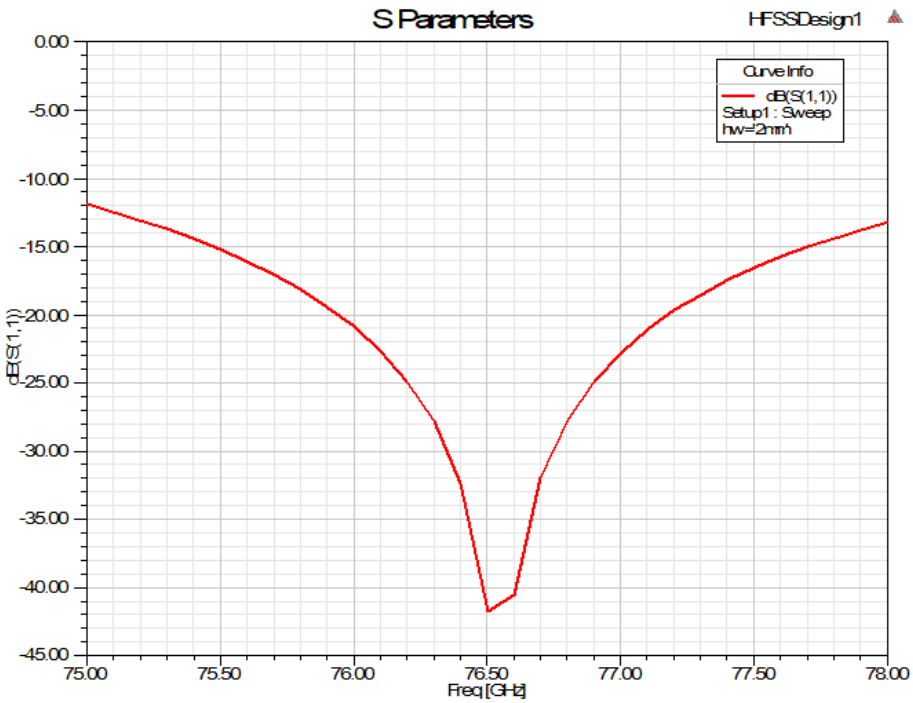

Figure 27. The Optimized S-Parameters with Provided Variables

This set of variables achieved a good impedance match at the operating frequency, 76.5 GHz. It also provides a more than 3 GHz (> 4%) 10-dB bandwidth. If the requirement is not restricted, the longitudinal dimension can be further shrunk down. The shortest *hw* value is 0.853 mm, which still provides a board 10-dB bandwidth, Figure 28.

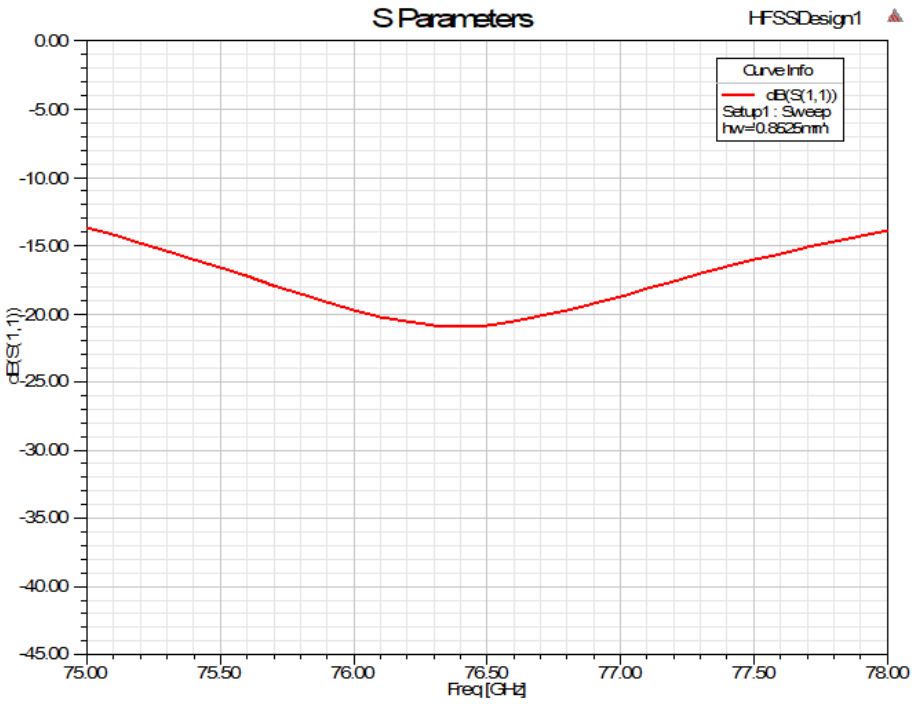

Figure 28. The Return Loss Value with Shortest Dimension

Cross-coupling is undesired between antennas in multiple-input and multiple-output (MIMO) communication systems. A comparative study of three types of cross-coupling was conducted. They are long-edge cross-talk (figure 29), short-edge cross-talk (figure 30), and orthogonal cross-talk (figure 31).

As shown in Figure 29, 30, and 31, purple lines are indicating cross coupling level

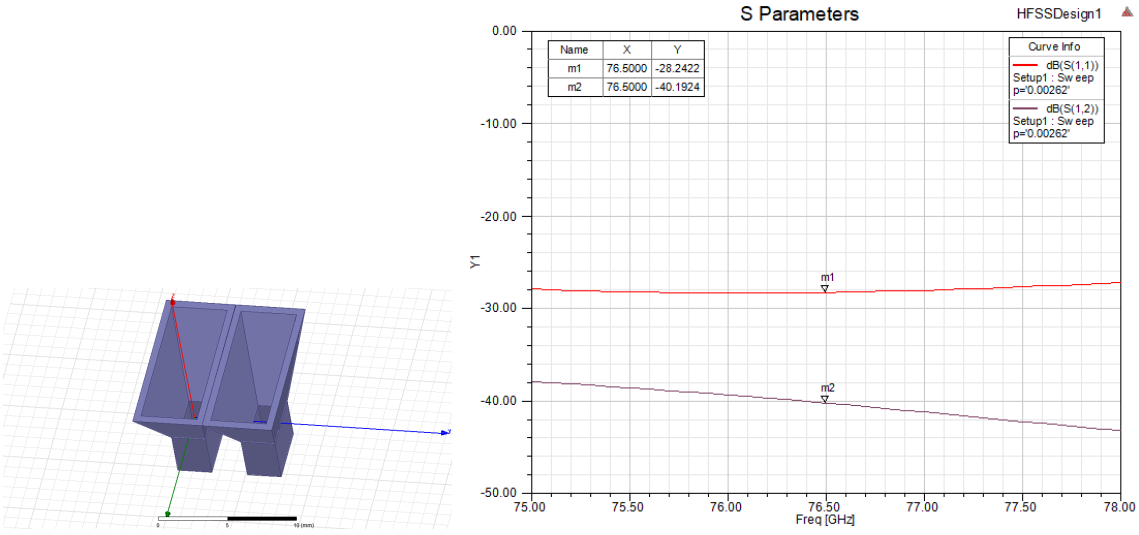

(a) (b)

Figure 29. Long-Edge Cross-Talk

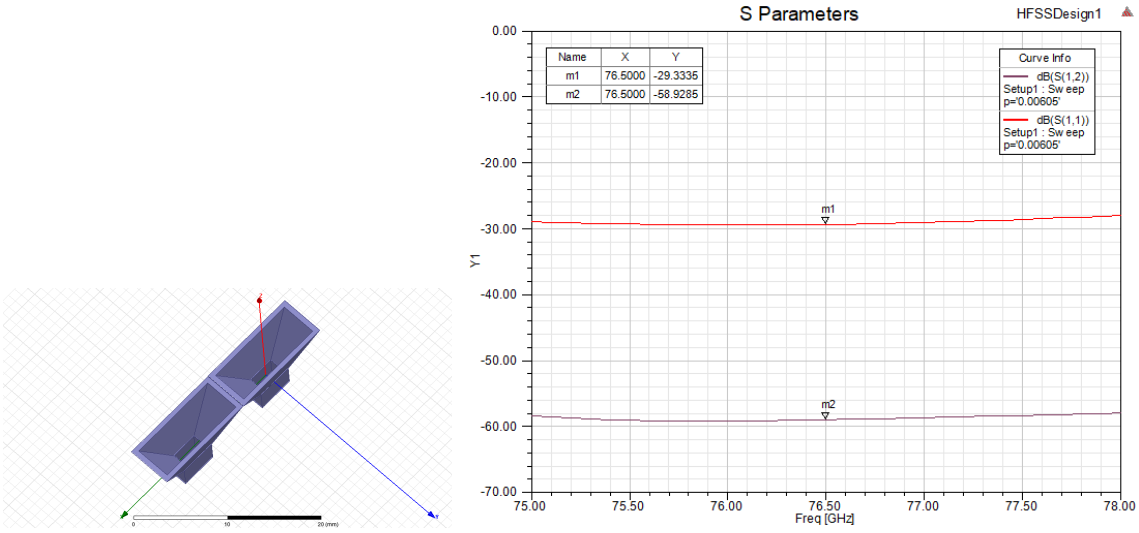

(a) (b)

Figure 30. Short-Edge Cross-Talk

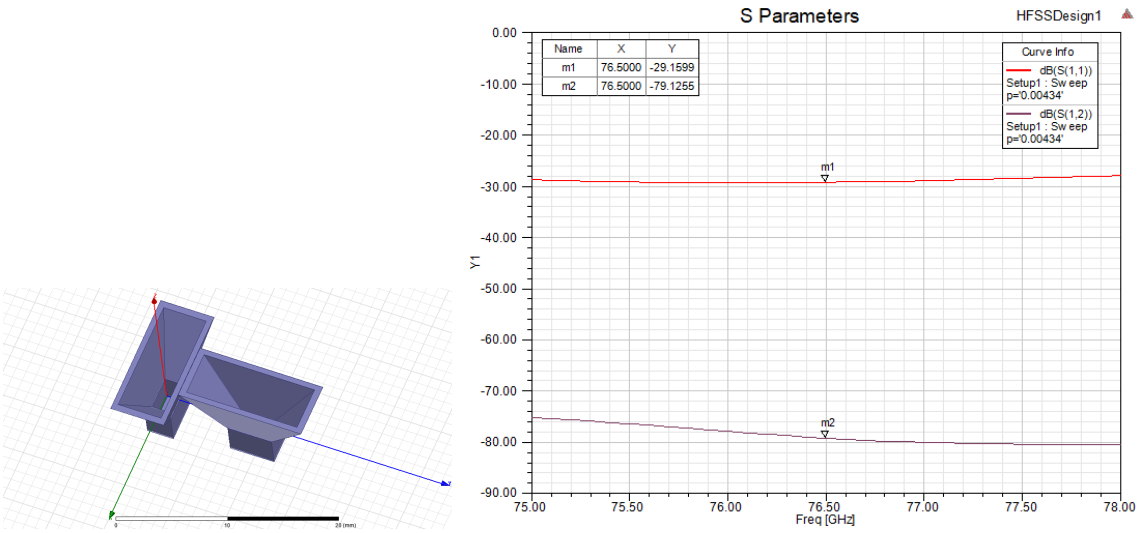

(a) (b)

Figure 31. Orthogonal Cross-Talk

of each type of configurations. The cross-talk level for long-edge, short-edge and orthogonal cases are around -40 dB, -60 dB and -80 dB correspondingly.

Comparing between long-edge case and short-edge case, the polarization of radiations are the same. The cross coupling level is affected by distance and gain patterns in E-plane and H-plane. The orthogonal case provides the lowest cross-talk level since the polarization from two horn antennas are perpendicular to each other. Thus, the orthogonal configuration is the ideal case for MIMO circuits.

3.2 Cavity Backed Slotted Antenna

Substrate integrate waveguides (SIW) has advantages of low profile and low cost. Which makes it as one type of candidate antenna for automotive multiple-input and multiple-output (MIMO) radars. The objective of this part is designing a Cavity

Backed Slotted Antenna [21] with an operating frequency at 5.30 GHz. Also study the impedance and gain properties from HFSS simulation.

The cavity resonance frequency is,

$$f = \frac{1}{2\sqrt{\mu\epsilon}}\sqrt{\left(\frac{m}{a}\right)^2 + \left(\frac{n}{b}\right)^2}. \tag{3.1}$$

For TE120 mode, $m = 1$ and $n = 2$. The experimental formula for the normalized width of the equivalent waveguide is [30]

$$\bar{a} = \xi_1 + \frac{\xi_2}{\frac{p}{d} + \frac{(\xi_1+\xi_2-\xi_3)}{(\xi_3-\xi_1)}}, \tag{3.2}$$

where

$$\begin{aligned} \xi_1 &= 1.0198 + \frac{0.3465}{\frac{a}{p} - 1.0684}, \\ \xi_2 &= -0.1183 - \frac{1.2729}{\frac{a}{p} - 1.2010}, \\ \xi_3 &= 1.0082 - \frac{0.9163}{\frac{a}{p} - 0.2152}. \end{aligned} \tag{3.3}$$

Therefore, the equivalent waveguide is

$$a_{RWG} = a\bar{a}. \tag{3.4}$$

The geometry [21] of CSA is presented in Figure 32. The model built in HFSS is shown in Fig 33.

From the HFSS simulation, $a = 37.46$ mm, $b = 47.30$ mm, $L_s = 20.81$ mm, and $W_s = 1.89$ mm. The 3-D radiation pattern is shown in Fig 34.

The return loss is finely tuned to the operating frequency at 5.30 GHz.It is shown in Fig 35, the -10-dB bandwidth is 61 MHz. The result suggests that the working

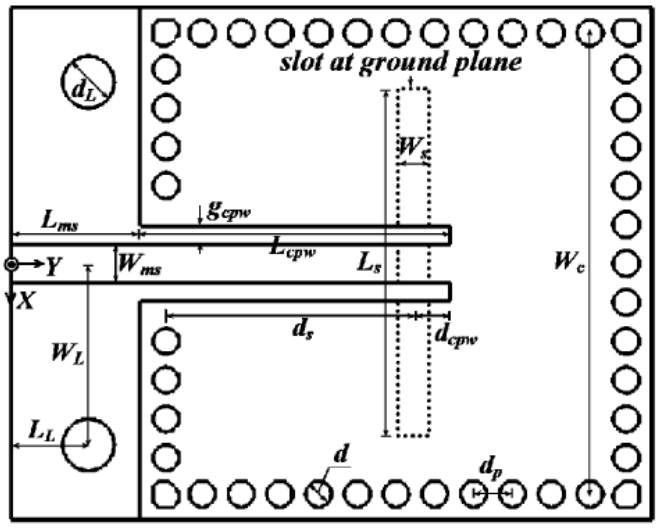

Figure 32. The Geometry of a Cavity-Backed Slotted Antenna.

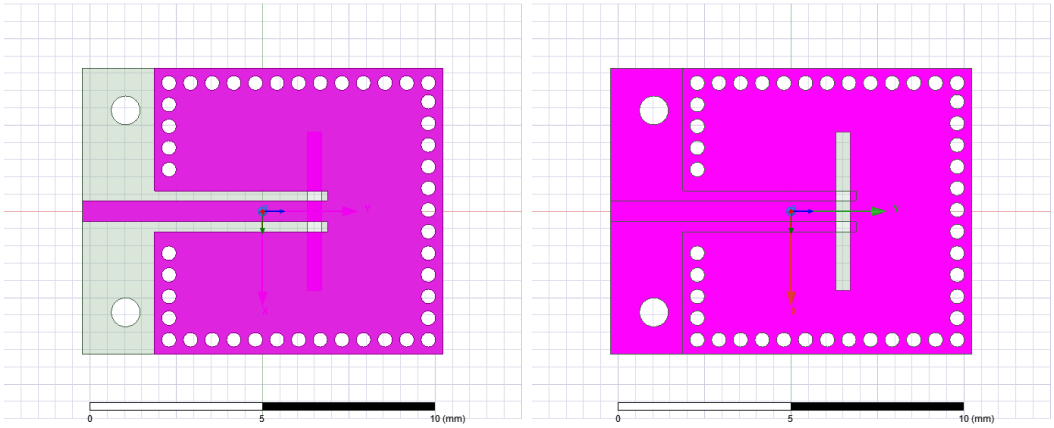

(a) (b)

Figure 33. The CSA Model Built in HFSS, (a) Back Side, (b) Front Side

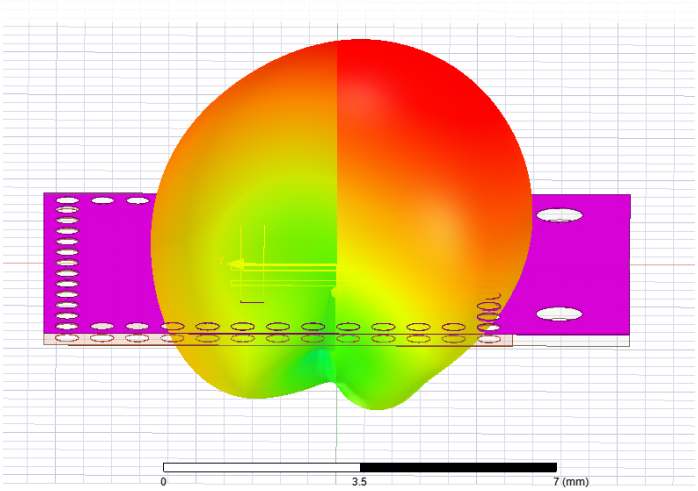

Figure 34. 3-D Radiation Pattern on Top of the Model

frequency of the CSA can be adjusted easily without modifying the fundamental design.

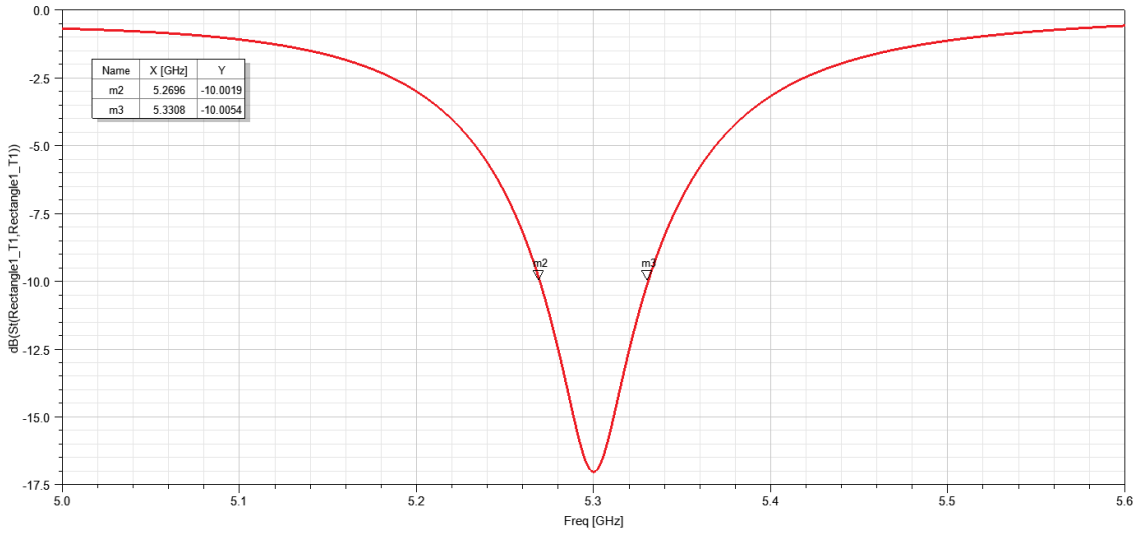

Figure 35. Plot of Return Loss (S11 Parameter)

Figure 36 denote the far-field radiation pattern of the antenna in E-plane and H-plane. On E-plane, the maximum gain 6.00 dB occurs at $\theta = -158°$. The 3-dB beamwidth on E-plane is 85°. On H-plane, the maximum gain 5.05 dB occurs at

$\theta = 180°$. And the 3-dB beamwidth is 80°. The front-to-back ratio is 16 dB for both E-plane and H-plane.

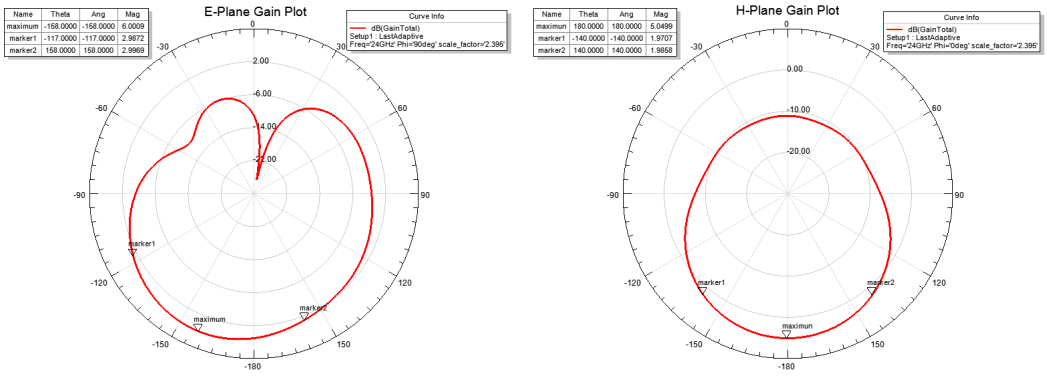

(a) (b)

Figure 36. Plots of Radiation Patterns, (a) E-Plane, (b) H-Plane.

Fig 37 is showing plots of polarization ratio in E-plane and H-plane. The maximum ratio on E-plane is 67.98 dB, which stands for a high purity in polarization. On H-plane, the polarization ratio varies from 0 dB to 30 dB in most directions.

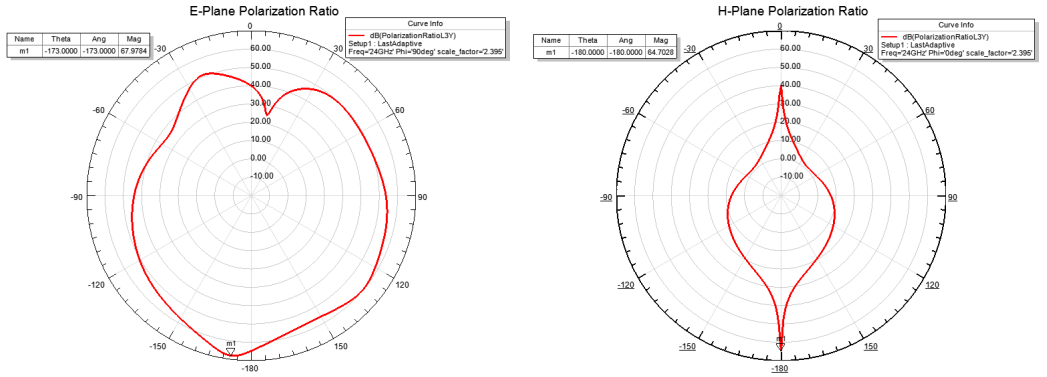

(a) (b)

Figure 37. The Polarization Ratio, (a) E-Plane, (b) H-Plane.

The antenna was originally operated at 10 GHz. By re-scaling the dimensions [22], we achieved a 0.35 GHz −10-dB bandwidth and maintained the gain to 6 dB.

3.3 Gain Improvement of Cavity Slotted Array

A cavity slotted array antenna (CSAA), shown in Figure 38, designed by a private company is studied in this section. It is a more sophisticated design than the one from Section 3.2. This cavity slotted array antenna has seven dielectric layers and eight conductive layers with the staggered arrangement, shown in Figure 39. The top conductive layer is the feeding part with co-planar waveguide. The bottom layer contains 3×16 T-shaped slots, shown in Figure 42 (a).

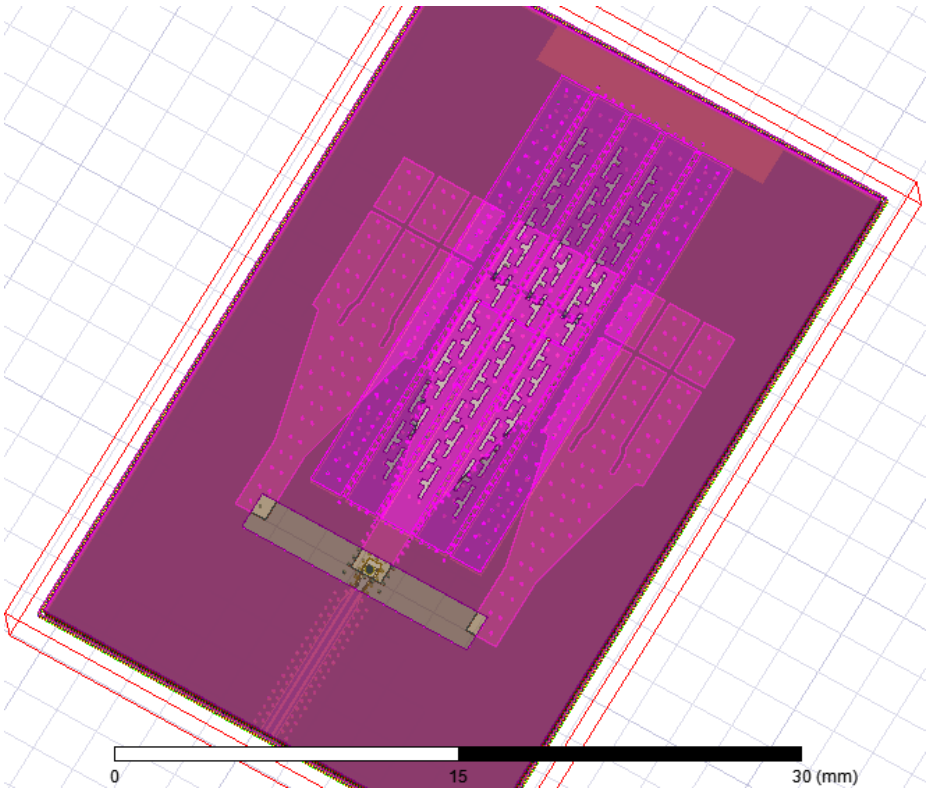

Figure 38. Original Cavity Slotted Array Model in HFSS

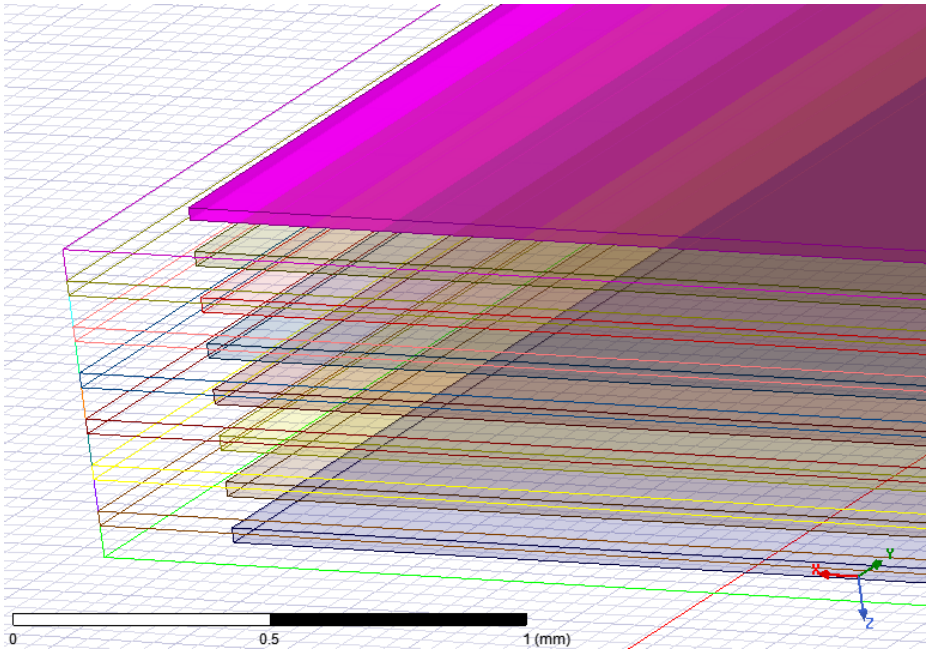

Figure 39. Different Layers of Cavity Slotted Array

The operating frequency of this antenna is 76.5 GHz. Figure 40 indicates gain plots in two principal planes. The original gain is 13.36 dB.

After studying the antenna by observing simulated electric fields, we were looking for performance improvements by modifying slots on the bottom layer.

Since the original 3-D model in HFSS is provided by the design company, a rebuilt bottom layer is needed in order to modify slots on it. The rebuilt model, shown in Figure 41, is identical to the original model in dimensions.

The first tested approach is substituting T-shaped slots with fractal slots. The comparison between two types of slots is shown in Figure 42. However, the maximum gain dropped to 10.43 dB, shown in Figure 43. The size of T-shaped slots is already a result of optimization. It is not easy to improve the gain by changing the shape of slots.

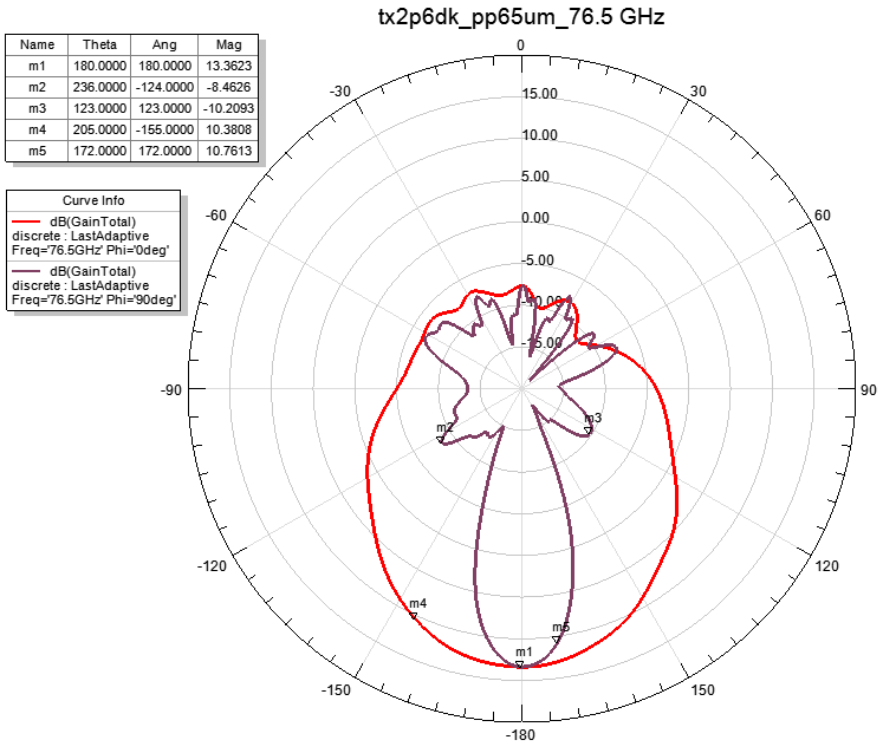

Figure 40. Original Gain Plot

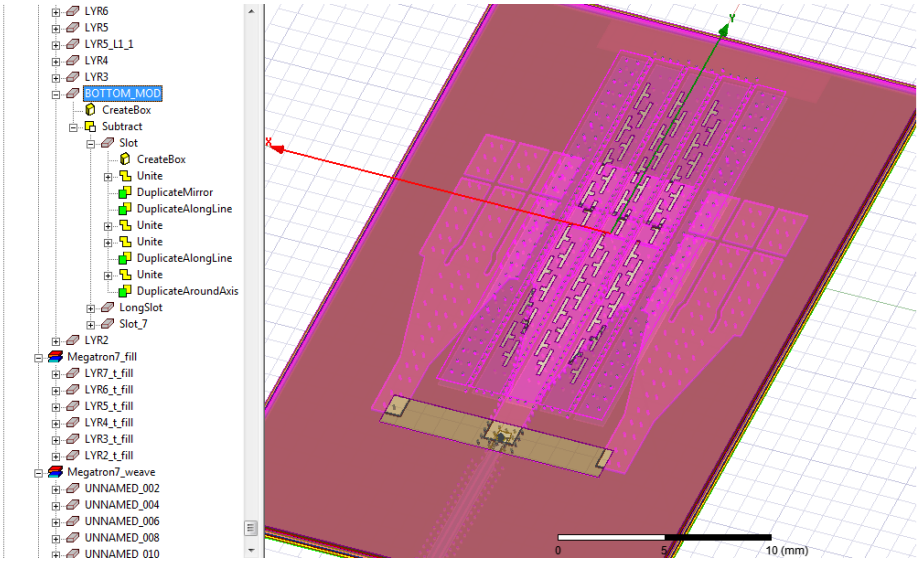

Figure 41. Remodeled Cavity Slotted Array

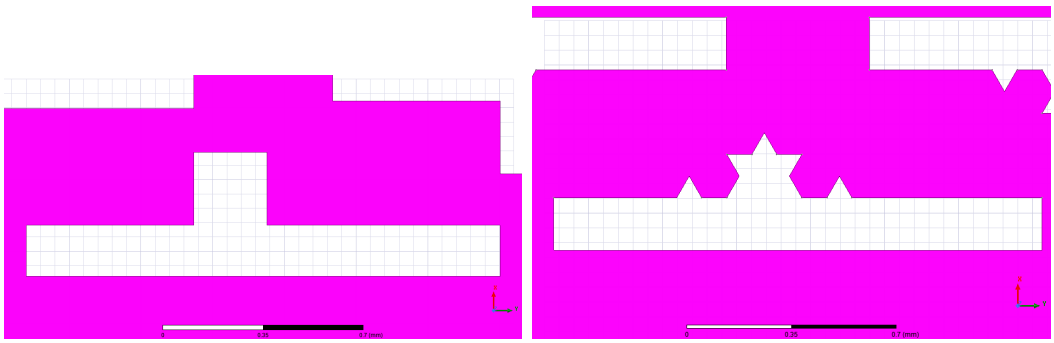

(a) (b)

Figure 42. View of Slots, (a) Original Slot, (b) Fractal Slot.

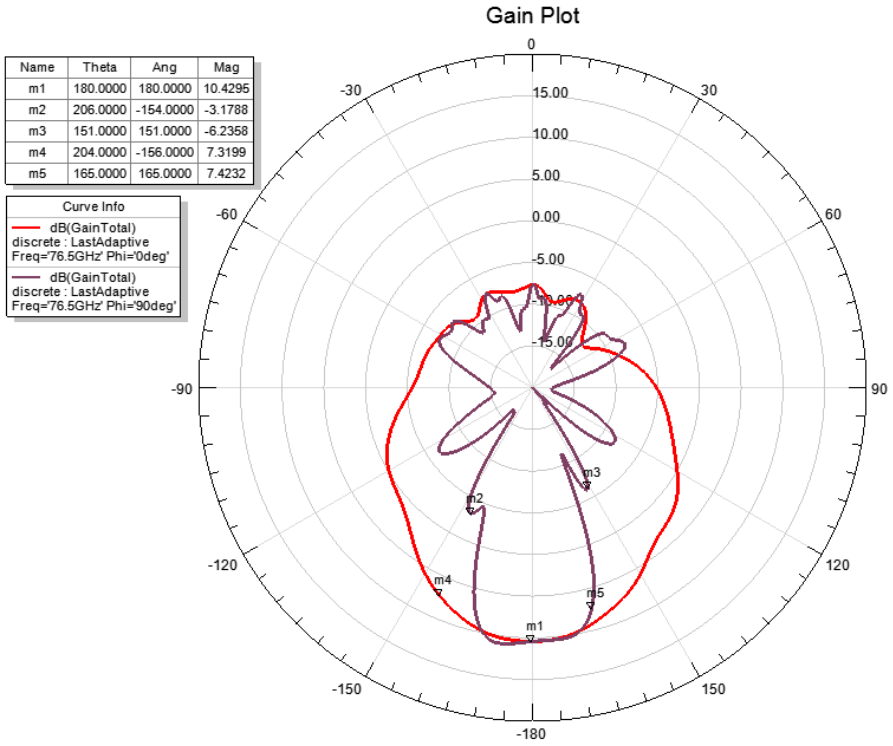

Figure 43. Gain Plot with Fractal Slots

The second modification approach is applied by adding more slots on top of dielectric cavities. In total, 6 sets of one and half T-shaped slots are added to the bottom layer. Figure 44 is the zoomed in view at revised part.

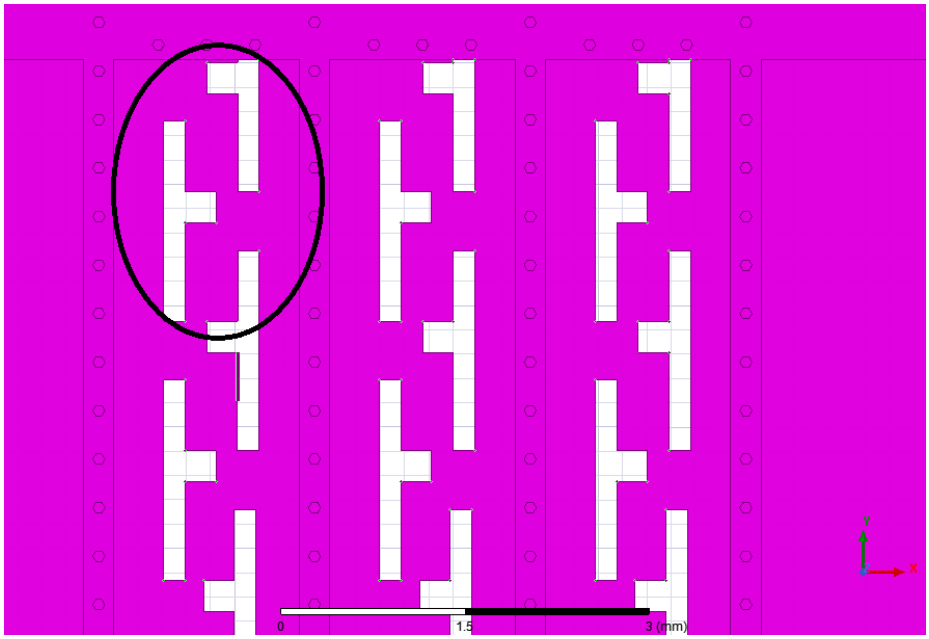

Figure 44. Additional Slots

With additional slots, the maximum gain is increased to 14.67 dB, shown in Figure 46.

One more approach, scaling the electric size of the device [22], is utilized to improve the gain and impedance performances. This procedure is conducted based on the additional-slot model. After scaling the original antenna size with a factor of 0.982, the results are improved. The updated gain is 15.59 dB, shown in Figure 47. Comparing to the original simulation result, the improvement of gain is 29.2% (2.23 dB). Figure 48 is the return loss plot over a frequency range from 75 GHz to 78 GHz.

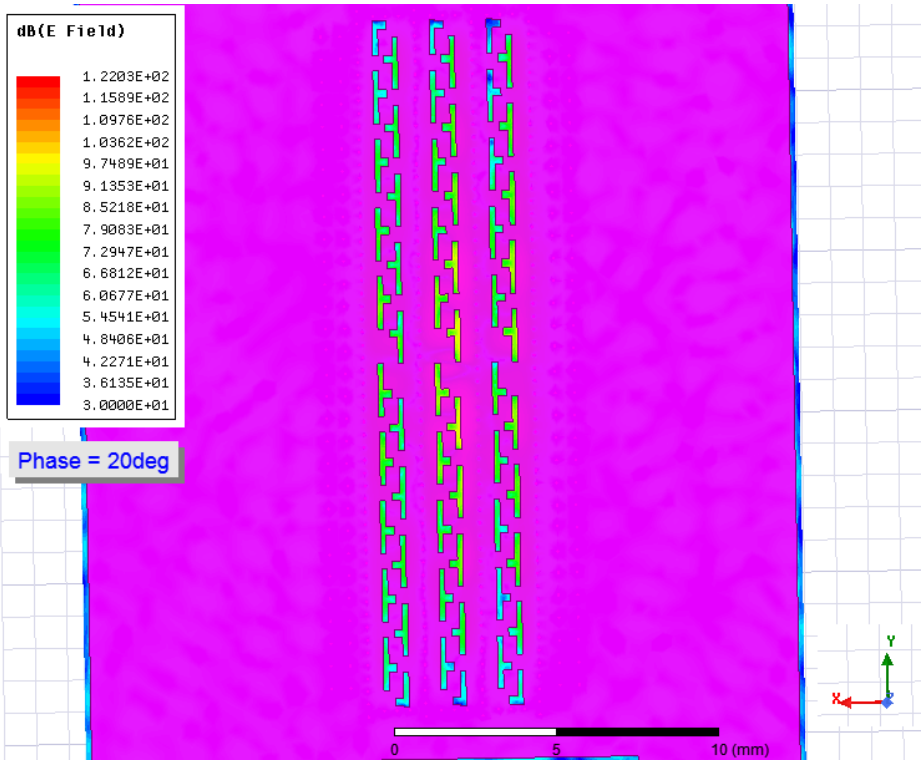

Figure 45. E-Field on Top of the Bottom Layer

3.4 Antenna Array Design with Phased Oscillators

The horn antenna is studied and prototyped using 3D printing technique, as shown in the Appendix. The cavity slotted array is investigated and applied to another specific commercial project. The cavity-backed slotted antenna from section 3.2 is selected as the radiating element to be integrated with the oscillator array on the same PCB. A seven-element one-dimensional array in Figure 49 is simulated to investigate beam steering.

After combining the antenna and oscillator arrays, radiation patterns are obtained from HFSS simulation, as shown in Figure 50. The scanning range is around $\pm 4°$,

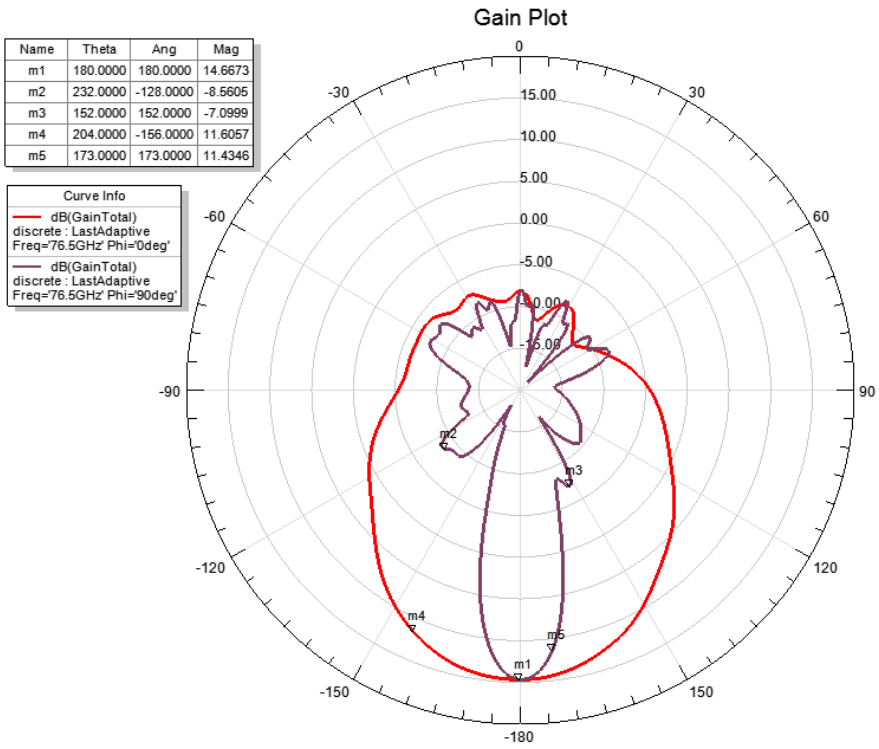

Figure 46. Gain Plot with Additional Slots

which is relatively narrow for many applications. There are multiple approaches to improve the scanning performance of the array.

3.5 Augmentation of Scanning Range

One approach to increase the scanning range is by adding frequency multipliers to the output of the oscillators [31–34]. By adding frequency multipliers to the circuit, the frequency and phase of each element are doubled. The radiation pattern and

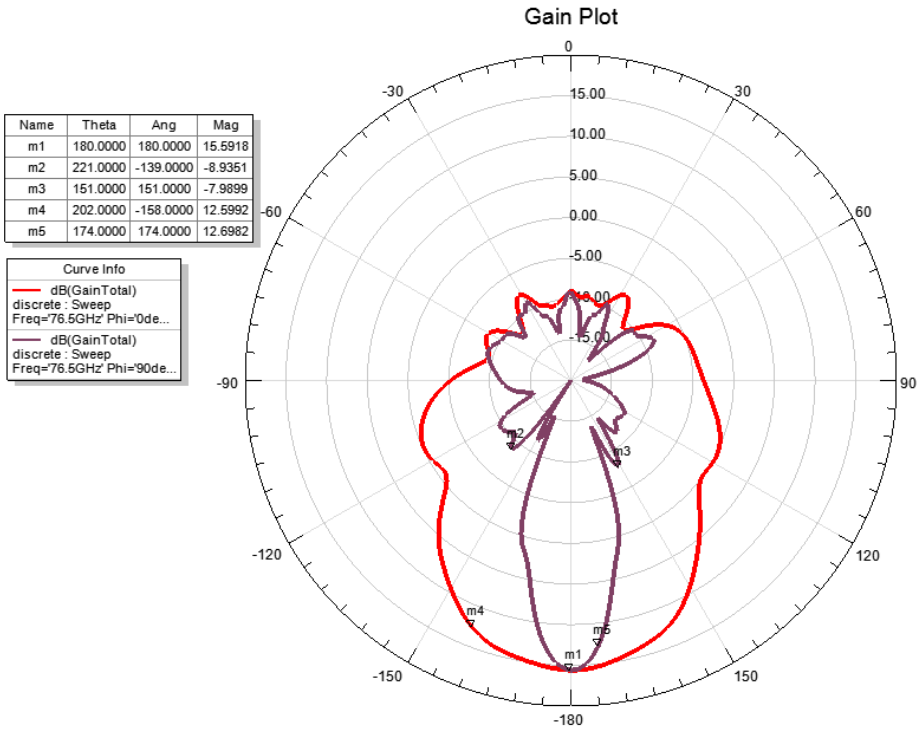

Figure 47. Gain Plot of the Optimized Model Applying Correct Loss Tangent Value

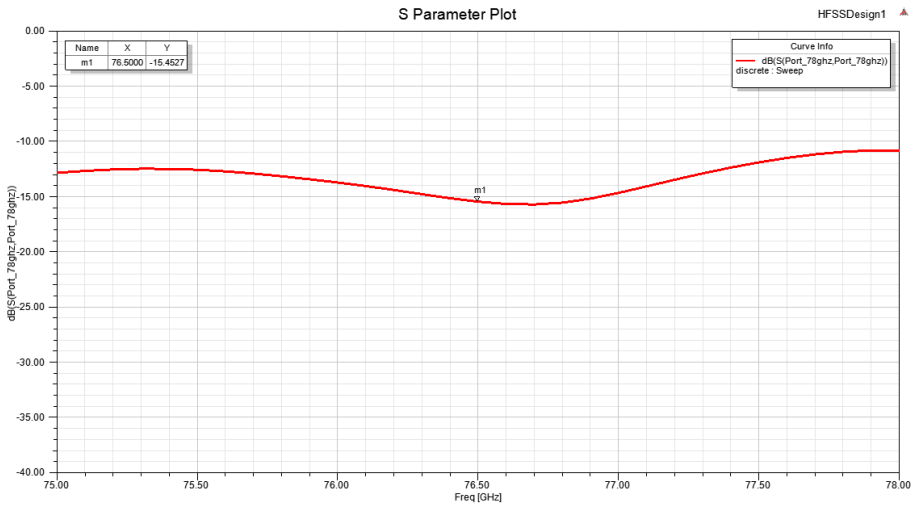

Figure 48. Return Loss Plot of the Optimized Model

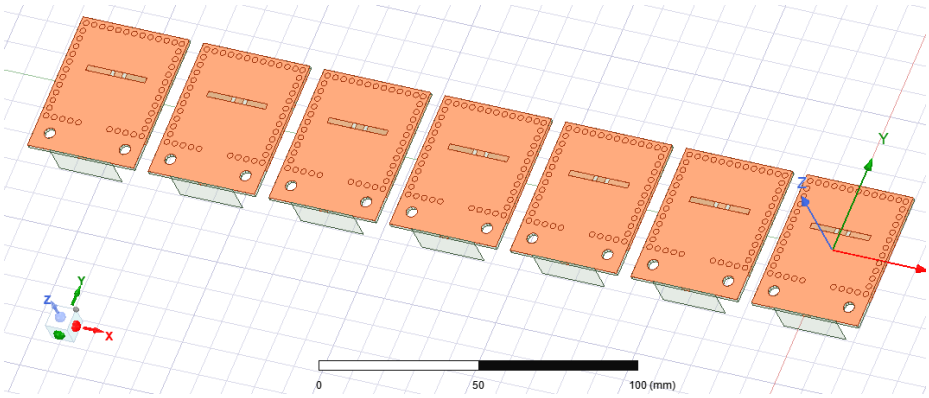

Figure 49. A Seven-Element One-Dimensional Antenna Array with the Radiation Elements Separated by $\frac{3}{4}\lambda$: $\lambda = 56.56$ Mm with Dielectric Constant of the Substrate as 2.2

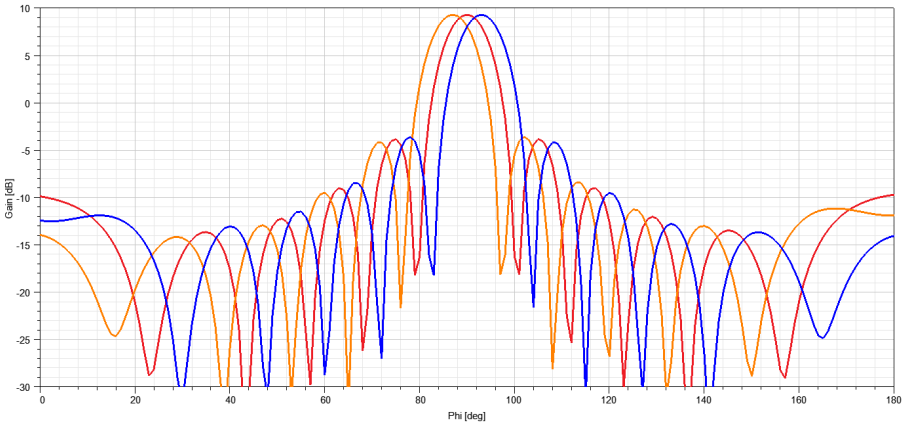

Figure 50. Radiation Patterns of Unsteered and Steered Beam Directions Drove by the Coupled Oscillators with Linear Phase Steps: Scanning Range $\pm 4°$

original scanning range of the uniform antenna array in Figure 49 is given by

$$\begin{aligned} |A(\Delta\phi)| &= \frac{1}{N}\left|1 + e^{j\Delta\phi} + e^{j2\Delta\phi} + \cdots + e^{j(N-1)\Delta\phi}\right| \\ &= \frac{1}{N}\left|\frac{1 - e^{jN\Delta\phi}}{1 - e^{j\Delta\phi}}\right| \\ &= \frac{1}{N}\left|\frac{\sin\frac{N\Delta\phi}{2}}{\sin\frac{\Delta\phi}{2}}\right| \end{aligned} \tag{3.5}$$

and

$$\theta_{scan} = \arcsin\left(\frac{2\Delta\phi}{3\pi}\right). \tag{3.6}$$

Due to the limitation of $\Delta\phi$ from Equation 2.9, the ideal maximum scan range is $\pm 19.5°$. With the doubled phases from oscillators, the updated equation for the scanning range is

$$\theta_{scan} = \arcsin\left(\frac{4\Delta\phi}{3\pi}\right). \tag{3.7}$$

And the updated ideal maximum scanning range is $\pm 41.8°$. Figure 51 shows the configuration of the array with frequency multipliers.

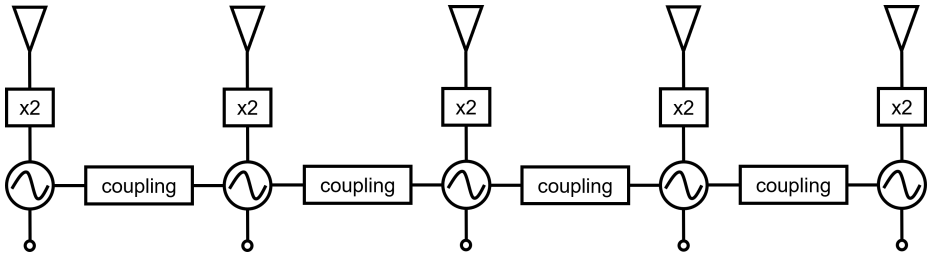

Figure 51. The Phased Array with Frequency Multipliers Implemented

In this project, the push-pull configuration, which is introduced in Section 2.2, presents an approach for frequency multiplication. Compared to the circuit previously described in the dissertation, the new version incorporates a frequency doubler in each oscillator, as detailed in Figure 52. Each oscillator operates at the fundamental frequency of 5.32 GHz, while the antennas operate at the second harmonic of 10.64 GHz, resulting in a doubling of the phase shift. Figure 53 demonstrates good agreement with the numerical prediction from Equation 3.7, with the phase shift doubled and an associated increment in the scanning range. Figure 54 further illustrates that the scanning range of the current design is increased to around $\pm 7.5°$. It is noted that the separation between radiation elements will affect the scanning performance. As shown in Figure 55, the cavity backed slotted antennas are scaled and separated by half wavelength. Comparing to the model dimensions from Section 3.2, the parameters are scaled to: $a = 8.8$ mm, $b = 11.11$ mm, $L_s = 4.89$ mm, and $W_s = 0.44$ mm.

The antenna array will be built on the same PCB board as the oscillator array. Roger RO3010 with a dielectric constant of 10.2 has been selected. The impedance performance is plotted in Figure 56, where the antenna operates at 10.65 GHz, and further tuning is needed for better return loss. Equation 3.7 is rewritten due to the element distance changes:

$$\theta_{scan} = \arcsin\left(\frac{2\Delta\phi}{\pi}\right). \tag{3.8}$$

Figure 57 depicts a scanning range of $\pm 10.5^{\circ}$, which represents a 40% improvement compared to the antenna array with $\frac{3}{4}$ wavelength element interval.

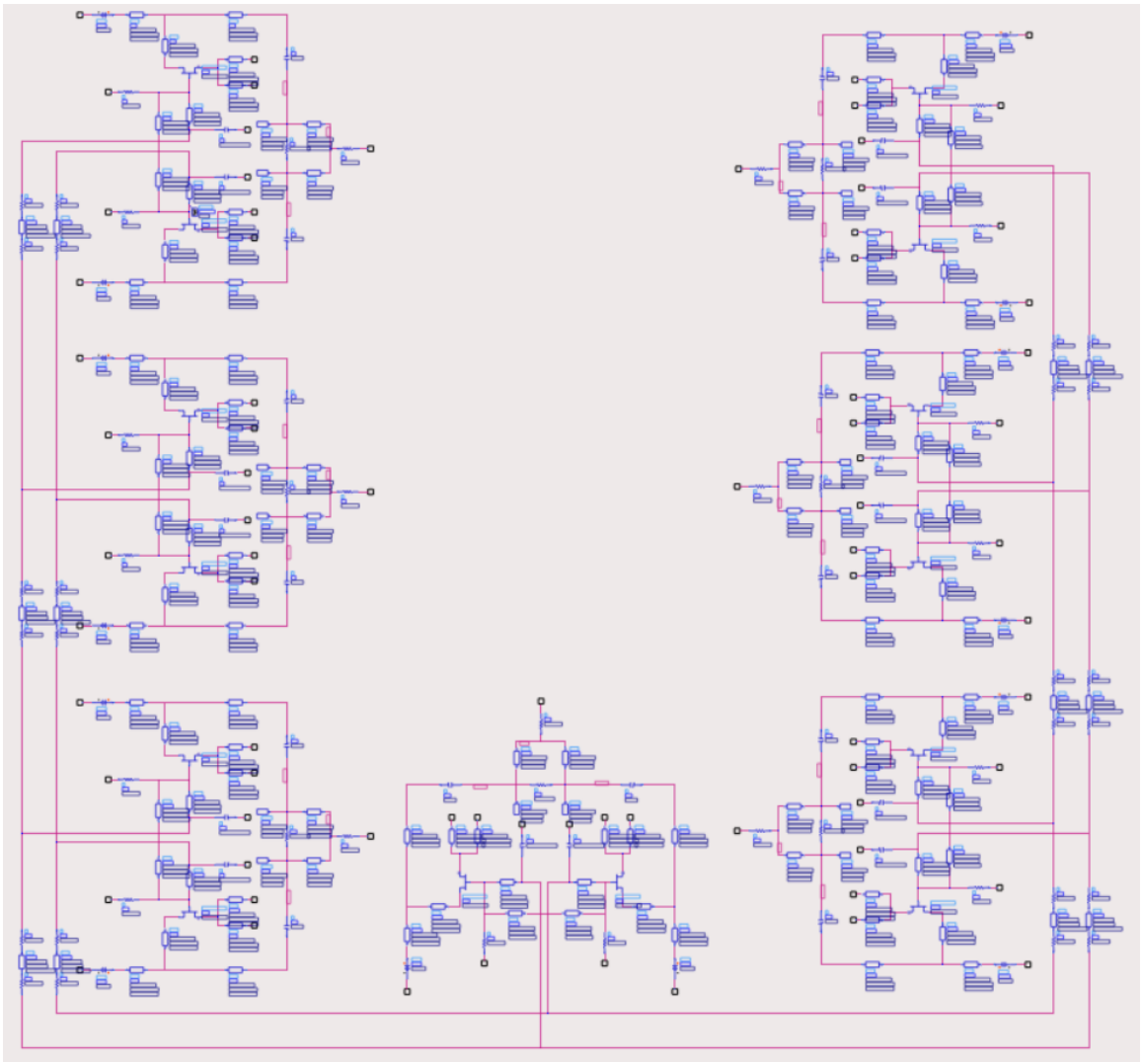

Figure 52. Schematic of Coupled Oscillator Array Using Push-Pull Configuration (Fundamental Resonant Frequency of Single Oscillator at 5.3 GHz, Radiation Elements Operating at 10.64 GHz Connected to the Load Port after Wilkinson Power Combiners)

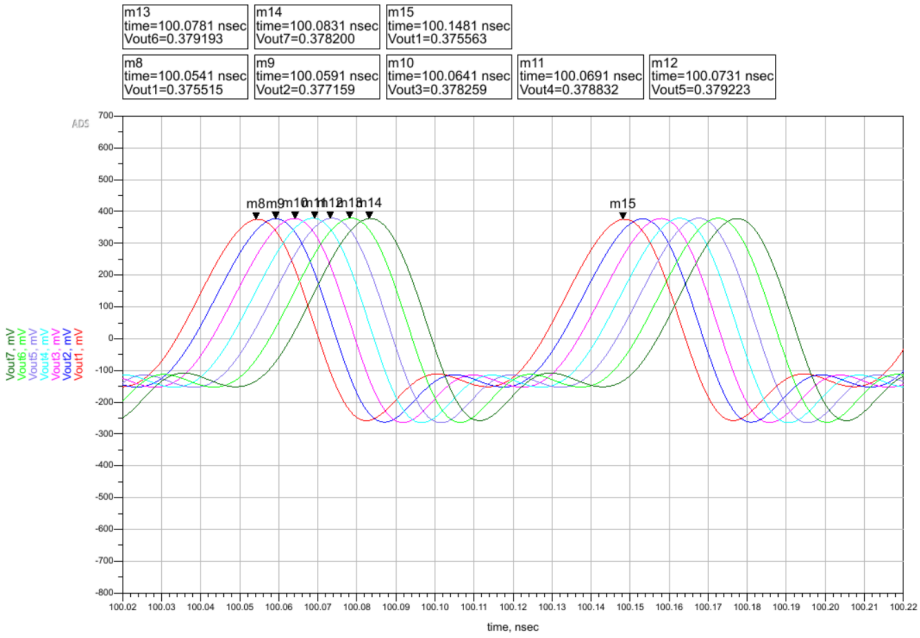

Figure 53. Augmented Phase Shift due to the Multiplied Frequency

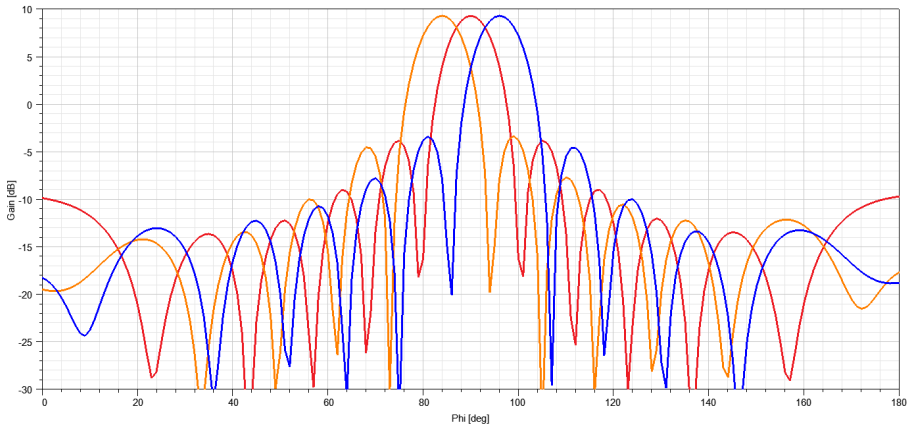

Figure 54. Radiation Patterns of Unsteered and Steered Beam Directions Driven by the Coupled Oscillators with Frequency Multipliers Added (Fundamental Resonant Frequency of Single Oscillator at 5.3 GHz, Antenna Array at Doubled Frequency Showing an Improved Scanning Range $\pm 7.5°$)

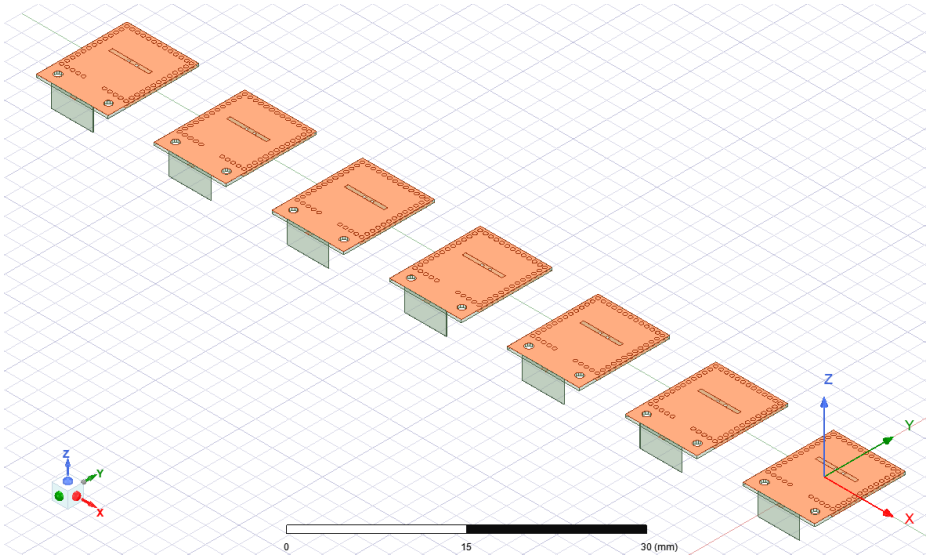

Figure 55. Antenna Array with the 10.64 GHz Scaled Radiation Elements Separated by $\frac{1}{2}$ Wavelength ($\lambda = 28.18$ Mm)

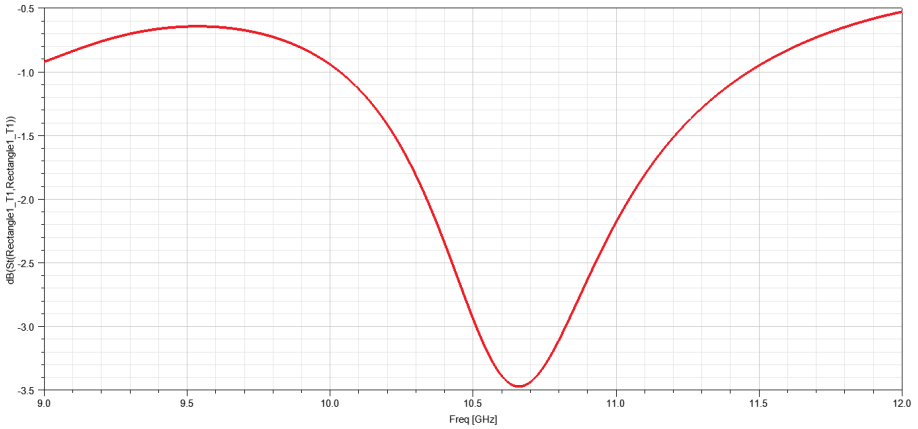

Figure 56. The Return Loss Performance of Individual Antenna that Scaled to Working at 10.65 GHz

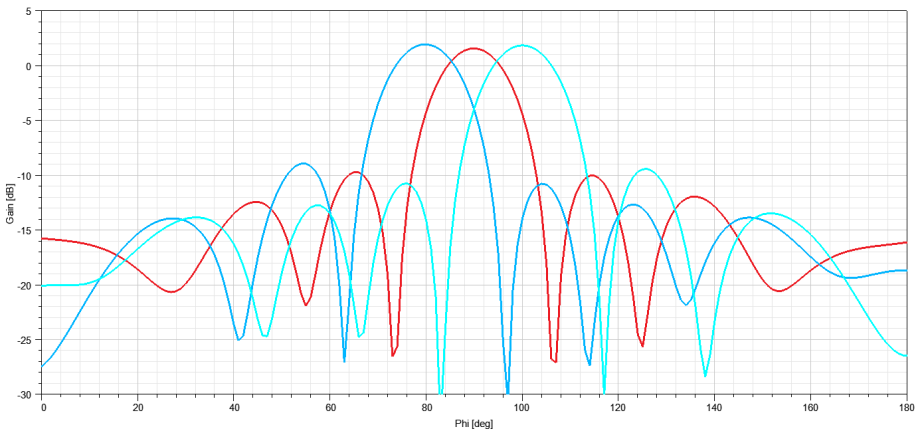

Figure 57. Radiation Patterns Augmented by Adjusting the Element Distance from $\frac{3}{4}\lambda$ to $\frac{1}{2}\lambda$ (Fundamental Resonant Frequency of Single Oscillator at 5.3 GHz, Antenna Array at Doubled Frequency: Scanning Range $\pm 10.5°$)

Chapter 4

CONCLUSION AND FUTURE WORK

In this document, a novel design is introduced for a phased array antenna that does not require individual phase shifters. The relationship between the Van der Pol (VDP) equation and resonant circuit is explored, and an approximate solution of the VDP equation is derived. The output performance of coupled oscillators is derived based on Adler's equation. Topics such as phased arrays without phase shifters, single-FET and push-pull oscillator designs, and antenna element designs are studied and discussed. The coupled oscillators, operating at 5.30 GHz, are utilized to build a reliable phased oscillator array to feed the scanning antenna array as a platform. The augmented scanning range is achieved by implementing frequency multipliers to the fundamental oscillators, resulting in a resonant frequency increase to 10.64 GHz and a doubling of the phase shift. This extends the scanning range and enables work on an antenna array with higher frequency. It is demonstrated that the operating frequency of the cavity backed slotted antenna can be modified with much flexibility.

This phased array design is verified analytically and through simulations in this document. It is shown that by coupling voltage-controlled oscillators together, the radiation beam direction can be steered without microelectromechanical systems (MEMS) phase shifters. This brings significant benefits, including but not limited to higher scanning speed, lower manufacturing and maintenance costs, lower system complexity, and space savings in compact designs.

The literature indicates that frequency multiplication techniques may enhance the phase-shift range of a coupled oscillator array. We propose to compare and contrast

the performance of traditional linear antenna arrays with nonlinear antenna arrays of various sizes (e.g., 16×16, 32×32, 64×64, etc.) in basic and sub-arrayed architectures through system level simulations. Fundamental trade-offs between gain, loss of the feed network, scan field of view, side-lobe level, front-to-back ratio, complexity, and cost will be determined in the future phase of the project. In addition, scanning errors and phase noise (flicking noise) are important topics to be studied.

REFERENCES

[1] Lisha Zhang et al. "On aperture coupling based compact system of lens enhanced phased array". en. In: *2012 IEEE 21st Conference on Electrical Performance of Electronic Packaging and Systems*. Tempe, AZ, USA: IEEE, Oct. 2012, pp. 292–295.

[2] B.K. Meadows et al. "Nonlinear antenna technology". en. In: *Proceedings of the IEEE* 90.5 (May 2002), pp. 882–897.

[3] Paul C. Matthews, Renato E. Mirollo, and Steven H. Strogatz. "Dynamics of a large system of coupled nonlinear oscillators". en. In: *Physica D: Nonlinear Phenomena* 52.2-3 (Sept. 1991), pp. 293–331.

[4] S.V. Hoeye, F. Ramirez, and A. Suarez. "Nonlinear optimization tools for the design of high-efficiency microwave oscillators". en. In: *IEEE Microwave and Wireless Components Letters* 14.5 (May 2004), pp. 189–191.

[5] Raj Senani et al. *Sinusoidal Oscillators and Waveform Generators using Modern Electronic Circuit Building Blocks*. en. Cham: Springer International Publishing, 2016.

[6] Paolo Rocca et al. "Unconventional Phased Array Architectures and Design Methodologies—A Review". en. In: *Proceedings of the IEEE* 104.3 (Mar. 2016), pp. 544–560.

[7] R. Adler. "A study of locking phenomena in oscillators". en. In: *Proceedings of the IEEE* 61.10 (1973), pp. 1380–1385.

[8] K. Kurokawa. "Injection locking of microwave solid-state oscillators". en. In: *Proceedings of the IEEE* 61.10 (1973), pp. 1386–1410.

[9] K. Stephan and W. Morgan. "Analysis of interinjection-locked oscillators for integrated phased arrays". en. In: *IEEE Transactions on Antennas and Propagation* 35.7 (July 1987), pp. 771–781.

[10] R.A. York. "Nonlinear analysis of phase relationships in quasi-optical oscillator arrays". en. In: *IEEE Transactions on Microwave Theory and Techniques* 41.10 (Oct. 1993), pp. 1799–1809.

[11] R.J. Pogorzelski, P.F. Maccarini, and R.A. York. "Continuum modeling of the dynamics of externally injection-locked coupled oscillator arrays". en. In: *IEEE*

Transactions on Microwave Theory and Techniques 47.4 (Apr. 1999), pp. 471–478.

[12] Ivan Straškraba and Otto Vejvoda. "Periodic solutions to abstract differential equations". en. In: *Czechoslovak Mathematical Journal* 23.4 (1973), pp. 635–669.

[13] John Mallet-Paret and George R. Sell. "The Poincaré–Bendixson Theorem for Monotone Cyclic Feedback Systems with Delay". en. In: *Journal of Differential Equations* 125.2 (Mar. 1996), pp. 441–489.

[14] Antoine Pauthier and Peter Poláčik. "Large-time behavior of solutions of parabolic equations on the real line with convergent initial data III: unstable limit at infinity". en. In: *Partial Differential Equations and Applications* 3.4 (Aug. 2022), p. 48.

[15] Jinjin Shen and L.W. Pearson. "A design for a two-dimensional coupled oscillator beam-steering antenna array". en. In: *IEEE Antennas and Wireless Propagation Letters* 2 (2003), pp. 360–362.

[16] Venkatesh Seetharam, Jinjin Shen, and L. Wilson Pearson. "Effect of Coupling Phase on Mutual Injection Locking Range in Coupled Oscillator Arrays". en. In: *IEEE Transactions on Antennas and Propagation* 57.5 (May 2009), pp. 1391–1398.

[17] Renaud Moussounda. "Analysis and Design of Coupled-Oscillator Arrays for Microwave Systems". en. In: (2013), p. 160.

[18] "Numerical Methods for Simulating Coupled-Oscillator Arrays". en. In: *Coupled-Oscillator Based Active-Array Antennas*. Hoboken, NJ, USA: John Wiley & Sons, Inc., July 2012, pp. 263–296.

[19] Yahya M. Tousi, Omeed Momeni, and Ehsan Afshari. "A Novel CMOS High-Power Terahertz VCO Based on Coupled Oscillators: Theory and Implementation". en. In: *IEEE Journal of Solid-State Circuits* 47.12 (Dec. 2012), pp. 3032–3042.

[20] S. Zhou et al. "E-Band 3-D Printed Antenna Fabrication and Measurement Using VNA and One-Side Frequency-Extender". en. In: *2018 IEEE 27th Conference on Electrical Performance of Electronic Packaging and Systems (EPEPS)*. San Jose, CA: IEEE, Oct. 2018, pp. 127–129.

[21] Qing Luo Guo. "Planar Slot Antenna Backed by Substrate Integrated Waveguide Cavity". In: *IEEE ANTENNAS AND WIRELESS PROPAGATION LETTERS* 7 (2008).

[22] Constantine A. Balanis, Kaiyue Zhang, and Craig R. Birtcher. "Geometrical Scale Modeling of Gain and Echo Area: Simulations, Measurements and Comparisons". In: *Applied Computational Electromagnetics Society Newsletter* 33 (2018), pp. 95–98.

[23] Nasser M Abbasi. "Solving the Van Der Pol nonlinear differential equation using first order approximation perturbation method". en. In: (2022), p. 11.

[24] Stephen Wirkus and Richard Rand. "The Dynamics of Two Coupled van der Pol Oscillators with Delay Coupling". en. In: *Nonlinear dynamic* 30.3 (2002), pp. 205–221.

[25] L Wilson Pearson, Jinjin Shen, and Xing Wang. "Coupled-Oscillator Phased Array Systems for Millimeter Wave Applications*". en. In: (2003), p. 4.

[26] S.A. Maas. "A GaAs MESFET Mixer with Very Low Intermodulation". en. In: *IEEE Transactions on Microwave Theory and Techniques* 35.4 (Apr. 1987), pp. 425–429.

[27] Jose Flores. "Design and analysis of an X-Band 2-Push Oscillator based on Complementary Split Ring Resonators". In: (July 2013).

[28] *ADS: Design Kit*. URL: www.renesas.com/us/en/document/pcs/agilent-ads-design-kit.

[29] A.G. Williamson. "Coaxially fed hollow probe in a rectangular waveguide". In: *IEE Proceedings H Microwaves, Antennas and Propagation* 132 (1985), p. 273.

[30] Yan Li. "Simulation and Experiment on SIW Slot Array Antennas". In: *IEEE MICROWAVE AND WIRELESS COMPONENTS LETTERS* 14 (2004).

[31] A. Alexanian, Heng-Chia Chang, and R.A. York. "Enhanced scanning range of coupled oscillator arrays utilizing frequency multipliers". en. In: *IEEE Antennas and Propagation Society International Symposium. 1995 Digest*. Vol. 2. Newport Beach, CA, USA: IEEE, 1995, pp. 1308–1310.

[32] R.J. Pogorzelski et al. "A seven-element S-band coupled-oscillator controlled agile-beam phased array". en. In: *IEEE Transactions on Microwave Theory and Techniques* 48.8 (Aug. 2000), pp. 1375–1384.

[33] J.I. Martinez-Lopez, R. Moussounda, and R.G. Rojas. "Non-reciprocal coupling network for beam-steering coupled oscillator arrays". en. In: *IET Microwaves, Antennas & Propagation* 5.8 (2011), p. 940.

[34] Z. Ghanian, A. Abdipour, and A. Ghorbani. "Nonlinear analysis, design, and implementation of a VCO in S frequency band". en. In: *Analog Integrated Circuits and Signal Processing* 49.2 (Nov. 2006), pp. 213–223.

APPENDIX A

WOLFRAM MATHEMATICA CODES OF VAN DER POL SOLUTIONS

No Resonance Case

```
In[29]:= initialPosition=1.5;
initialSpeed=Sqrt[4-initialPosition^2];
In[31]:= x=x0 Cos[t]+v0 Sin[t]+\[Alpha]((v0 (v0^2-3))/8 Cos[t
    ]+3/8 x0(x0^2-3)Sin[t]+(v0 (3-v0^2))/8 Cos[3 t]+(x0 (3-x0
    ^2))/8 Sin[3 t])
Out[31]= x0 Cos[t]+v0 Sin[t]+\[Alpha] (1/8 v0 (-3+v0^2) Cos[t
    ]+1/8 v0 (3-v0^2) Cos[3 t]+3/8 x0 (-3+x0^2) Sin[t]+1/8 x0
    (3-x0^2) Sin[3 t])
In[32]:= x\[Alpha]=x/.{\[Alpha]->0.01, x0->initialPosition,v0
    ->initialSpeed}
Out[32]= 1.5 Cos[t]+1.32288 Sin[t]+0.01 (-0.206699 Cos[t
    ]+0.206699 Cos[3 t]-0.421875 Sin[t]+0.140625 Sin[3 t])
In[33]:= v\[Alpha]=D[x,t]/.{\[Alpha]->0.01, x0->
    initialPosition,v0->initialSpeed}
Out[33]= 1.32288 Cos[t]-1.5 Sin[t]+0.01 (-0.421875 Cos[t
    ]+0.421875 Cos[3 t]+0.206699 Sin[t]-0.620098 Sin[3 t])
In[1]:= data=Table[{x\[Alpha], v\[Alpha]},{t,0,60,0.01}];
In[35]:= p=ListPlot[data,AxesLabel->{"x(t)","v(t)"},PlotLabel
    ->"Phase plane for I.C. x(0)="<>ToString[initialPosition
    ]<>" and v(0)="<>ToString[initialSpeed]<>" \[Alpha]=0.01"
    ];
In[36]:= p2=Graphics[{PointSize[0.03],Point[{initialPosition,
    initialSpeed}]}];
In[37]:= Show[{p,p2},AspectRatio->1]
```

Resonance Case

```
Resonance
initialPosition=1.5;
initialSpeed=Sqrt[4-initialPosition^2];
(*initialPosition=1.5;
initialSpeed=Sqrt[4-initialPosition^2];*)
perturbationf=2;
x=x0 Cos[t]+v0 Sin[t]+\[Alpha](-(v0^3/32)+(v0 x0^2)/32+1/8 v0
    )Cos[t]-\[Alpha]/32 x0(5 v0^2-7 x0^2+16)Sin[t]+\[Alpha] t
    (1/2 x0(1-(x0^2+v0^2)/4)Cos[t])+\[Alpha] t(1/2 v0(1-(v0^2-
    x0^2)/4)Sin[t])+\[Alpha]/8 v0((v0^2-x0^2)/4-1)Cos[3t]+\[
    Alpha]/8 x0((3 v0^2-x0^2)/4)Sin[3t];
x\[Alpha]=x/.{\[Alpha]->perturbationf, x0->initialPosition,v0
    ->initialSpeed}
```

```
v\[Alpha]=D[x,t]/.{\[Alpha]->perturbationf, x0->
    initialPosition,v0->initialSpeed}
data=Table[{x\[Alpha], v\[Alpha]},{t,0,60,0.01}];
p=ListPlot[data,AxesLabel->{"x(t)","v(t)"},PlotLabel->"Phase␣
    plane␣for␣I.C.␣x(0)="<>ToString[initialPosition]<>"␣and␣v
    (0)="<>ToString[initialSpeed]<>"␣\[Alpha]=␣"<>ToString[
    perturbationf]];
p2=Graphics[{PointSize[0.03],Point[{initialPosition,
    initialSpeed}]}];
Show[{p,p2},AspectRatio->1]
Out[465]= 0. +1.87206 Cos[t]-0.372059 Cos[3 t]+0.479126 Sin[t
    ]+1.48824 t Sin[t]+0.28125 Sin[3 t]
Out[466]= 0. +0.479126 Cos[t]+1.48824 t Cos[t]+0.84375 Cos[3
    t]-0.383824 Sin[t]+1.11618 Sin[3 t]
Out[470]=
In[431]:= Plot[v\[Alpha],{t,0,400},PlotRange->5]
```

APPENDIX B

RUNGE–KUTTA METHODS WITH MATLAB

```
h=2.6e-12;
omega0=5.35e9*2*pi;
kapa0=0.5;
Qfactor=18;
delta_omega=20e6*2*pi;
end_time=12e-8;

%initial phase in degree
phase_no(1)=90;
phase_no(2)=60;
phase_no(3)=30;
phase_no(4)=0;
phase_no(5)=-30;
phase_no(6)=-60;
phase_no(7)=-90;

N_element=7;

N=floor(end_time/h);
omega1=omega0+delta_omega;
omega7=omega0-delta_omega;

% Pre-calculation of locking range
locking_range0=kapa0*omega0/2/Qfactor;
locking_range1=kapa0*omega1/2/Qfactor;
locking_range7=kapa0*omega7/2/Qfactor;

theta=zeros(N_element,N+1);
theta(:,1)=phase_no'*pi/180;
time=linspace(0,end_time,N+1);
k1=zeros(N_element,N);
k2=zeros(N_element,N);
k3=zeros(N_element,N);
k4=zeros(N_element,N);
phase_shift=zeros(N_element-1,N);



for i=2:N+1
    k1(1,i-1)=omega1-locking_range1*sin(theta(1,i-1)-theta(2,
        i-1));
```

```
k1(2,i-1)=omega0-locking_range0*(sin(theta(2,i-1)-theta
    (1,i-1))+sin(theta(2,i-1)-theta(3,i-1)));
k1(3,i-1)=omega0-locking_range0*(sin(theta(3,i-1)-theta
    (2,i-1))+sin(theta(3,i-1)-theta(4,i-1)));
k1(4,i-1)=omega0-locking_range0*(sin(theta(4,i-1)-theta
    (3,i-1))+sin(theta(4,i-1)-theta(5,i-1)));
k1(5,i-1)=omega0-locking_range0*(sin(theta(5,i-1)-theta
    (4,i-1))+sin(theta(5,i-1)-theta(6,i-1)));
k1(6,i-1)=omega0-locking_range0*(sin(theta(6,i-1)-theta
    (5,i-1))+sin(theta(6,i-1)-theta(7,i-1)));
k1(7,i-1)=omega7-locking_range7*sin(theta(7,i-1)-theta(6,
    i-1));

k2(1,i-1)=omega1-locking_range1*sin(theta(1,i-1)-theta(2,
    i-1)+(k1(1,i-1)-k1(2,i-1))*h/2);
k2(2,i-1)=omega0-locking_range0*(sin(theta(2,i-1)-theta
    (1,i-1)+(k1(2,i-1)-k1(1,i-1))*h/2)+sin(theta(2,i-1)-
    theta(3,i-1)+(k1(2,i-1)-k1(3,i-1))*h/2));
k2(3,i-1)=omega0-locking_range0*(sin(theta(3,i-1)-theta
    (2,i-1)+(k1(3,i-1)-k1(2,i-1))*h/2)+sin(theta(3,i-1)-
    theta(4,i-1)+(k1(3,i-1)-k1(4,i-1))*h/2));
k2(4,i-1)=omega0-locking_range0*(sin(theta(4,i-1)-theta
    (3,i-1)+(k1(4,i-1)-k1(3,i-1))*h/2)+sin(theta(4,i-1)-
    theta(5,i-1)+(k1(4,i-1)-k1(5,i-1))*h/2));
k2(5,i-1)=omega0-locking_range0*(sin(theta(5,i-1)-theta
    (4,i-1)+(k1(5,i-1)-k1(4,i-1))*h/2)+sin(theta(5,i-1)-
    theta(6,i-1)+(k1(5,i-1)-k1(6,i-1))*h/2));
k2(6,i-1)=omega0-locking_range0*(sin(theta(6,i-1)-theta
    (5,i-1)+(k1(6,i-1)-k1(5,i-1))*h/2)+sin(theta(6,i-1)-
    theta(7,i-1)+(k1(6,i-1)-k1(7,i-1))*h/2));
k2(7,i-1)=omega7-locking_range7*sin(theta(7,i-1)-theta(6,
    i-1)+(k1(7,i-1)-k1(6,i-1))*h/2);

k3(1,i-1)=omega1-locking_range1*sin(theta(1,i-1)-theta(2,
    i-1)+(k2(1,i-1)-k2(2,i-1))*h/2);
k3(2,i-1)=omega0-locking_range0*(sin(theta(2,i-1)-theta
    (1,i-1)+(k2(2,i-1)-k2(1,i-1))*h/2)+sin(theta(2,i-1)-
    theta(3,i-1)+(k2(2,i-1)-k2(3,i-1))*h/2));
k3(3,i-1)=omega0-locking_range0*(sin(theta(3,i-1)-theta
    (2,i-1)+(k2(3,i-1)-k2(2,i-1))*h/2)+sin(theta(3,i-1)-
    theta(4,i-1)+(k2(3,i-1)-k2(4,i-1))*h/2));
k3(4,i-1)=omega0-locking_range0*(sin(theta(4,i-1)-theta
```

```
        (3,i-1)+(k2(4,i-1)-k2(3,i-1))*h/2)+sin(theta(4,i-1)-
        theta(5,i-1)+(k2(4,i-1)-k2(5,i-1))*h/2));
    k3(5,i-1)=omega0-locking_range0*(sin(theta(5,i-1)-theta
        (4,i-1)+(k2(5,i-1)-k2(4,i-1))*h/2)+sin(theta(5,i-1)-
        theta(6,i-1)+(k2(5,i-1)-k2(6,i-1))*h/2));
    k3(6,i-1)=omega0-locking_range0*(sin(theta(6,i-1)-theta
        (5,i-1)+(k2(6,i-1)-k2(5,i-1))*h/2)+sin(theta(6,i-1)-
        theta(7,i-1)+(k2(6,i-1)-k2(7,i-1))*h/2));
    k3(7,i-1)=omega7-locking_range7*sin(theta(7,i-1)-theta(6,
        i-1)+(k2(7,i-1)-k2(6,i-1))*h/2);

    k4(1,i-1)=omega1-locking_range1*sin(theta(1,i-1)-theta(2,
        i-1)+(k3(1,i-1)-k3(2,i-1))*h);
    k4(2,i-1)=omega0-locking_range0*(sin(theta(2,i-1)-theta
        (1,i-1)+(k3(2,i-1)-k3(1,i-1))*h)+sin(theta(2,i-1)-
        theta(3,i-1)+(k3(2,i-1)-k3(3,i-1))*h));
    k4(3,i-1)=omega0-locking_range0*(sin(theta(3,i-1)-theta
        (2,i-1)+(k3(3,i-1)-k3(2,i-1))*h)+sin(theta(3,i-1)-
        theta(4,i-1)+(k3(3,i-1)-k3(4,i-1))*h));
    k4(4,i-1)=omega0-locking_range0*(sin(theta(4,i-1)-theta
        (3,i-1)+(k3(4,i-1)-k3(3,i-1))*h)+sin(theta(4,i-1)-
        theta(5,i-1)+(k3(4,i-1)-k3(5,i-1))*h));
    k4(5,i-1)=omega0-locking_range0*(sin(theta(5,i-1)-theta
        (4,i-1)+(k3(5,i-1)-k3(4,i-1))*h)+sin(theta(5,i-1)-
        theta(6,i-1)+(k3(5,i-1)-k3(6,i-1))*h));
    k4(6,i-1)=omega0-locking_range0*(sin(theta(6,i-1)-theta
        (5,i-1)+(k3(6,i-1)-k3(5,i-1))*h)+sin(theta(6,i-1)-
        theta(7,i-1)+(k3(6,i-1)-k3(7,i-1))*h));
    k4(7,i-1)=omega7-locking_range7*sin(theta(7,i-1)-theta(6,
        i-1)+(k3(7,i-1)-k3(6,i-1))*h);

    theta(:,i)=theta(:,i-1)+(k1(:,i-1)+2*k2(:,i-1)+2*k3(:,i
        -1)+k4(:,i-1))*h/6;
    phase_shift(:,i-1)=(theta(1:N_element-1,i)-theta(2:
        N_element,i))*180/pi;
end

phase_step=(theta(:,2:N+1)-theta(:,1:N))*180/pi;

line_width=2;
figure;
```

```
han1=plot(time(2:N+1),phase_shift(1,:),"LineWidth",line_width
    );
hold on
han2=plot(time(2:N+1),phase_shift(2,:),"Marker","+","
    MarkerIndices",1:floor(N/30):N,"LineWidth",line_width);
han3=plot(time(2:N+1),phase_shift(3,:),"LineStyle","--","
    LineWidth",line_width);
han4=plot(time(2:N+1),phase_shift(4,:),"LineStyle",":","
    LineWidth",line_width);
han5=plot(time(2:N+1),phase_shift(5,:),"LineStyle","-.","
    MarkerIndices",1:floor(N/30):N,"LineWidth",line_width);
han6=plot(time(2:N+1),phase_shift(6,:),"Marker","x","
    MarkerIndices",1:floor(N/30):N,"LineWidth",line_width);
legend([han1 han2 han3 han4 han5 han6],{'\theta_1-\theta_2','
    \theta_2-\theta_3','\theta_3-\theta_4','\theta_4-\theta_5'
    ,'\theta_5-\theta_6','\theta_6-\theta_7'},"Location","best
    ")
title("Phase Shifts between Oscillators");
ylabel("Phase Shifts in Degree")
xlabel("Time in Second")
hold off
```

APPENDIX C

PROTOTYPING OF THE HORN ANTENNA

The prototypes of the horn antenna were built and measured at the Arizona State University facility. The 3D printed horn antennas were made of conventional ABS material, which is non-conductive. We then coated the horns with copper in the lab, using various methods of electroplating. A graphite-acetone mixture was utilized as a conducting base because acetone can etch the ABS material and allow the graphite to adhere to the ABS surface. The resulting copper electroplated horn antennas with WR-12 connectors are shown in Figure 58.

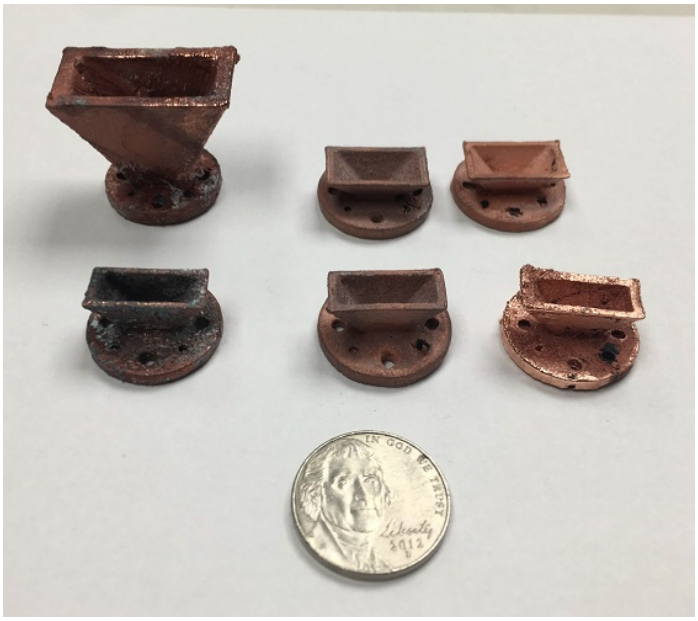

Figure 58. Copper Electroplated Horn Antennas with WR-12 Connector

The insertion loss and gain are presented in Figure 59 and Figure 60, respectively, and are compared to the values obtained from HFSS simulations and analytic calculations. However, due to surface roughness and fabrication variance, there are some differences between the measured and simulated values.

The results demonstrate that electroplating 3D printed horn antennas yields good agreement with simulation results at E-band frequencies. This process could also be applied to other types of antennas in the future, particularly for low-cost, small, and irregular antennas.

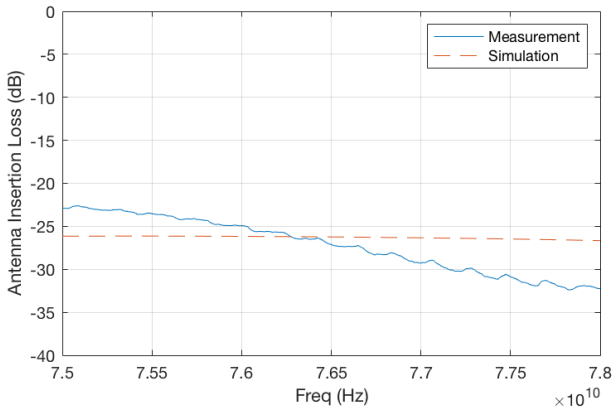

Figure 59. Comparison of HFSS Simulated and Measurement Insertion Loss

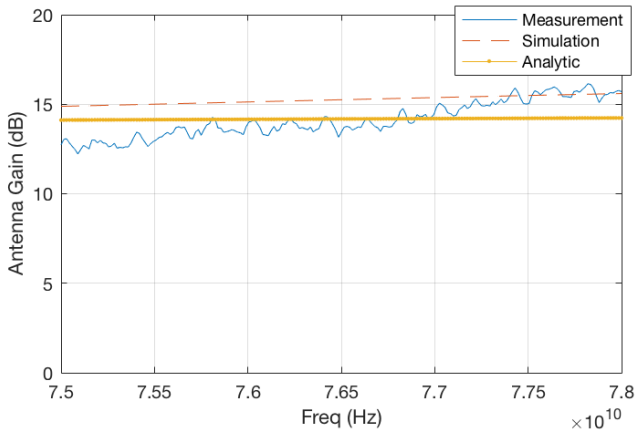

Figure 60. Comparison of HFSS Simulated, Measurement and Analytic Solution of Antenna Gain